eman ta zabal zazu
Universidad del País Vasco   Euskal Herriko Unibertsitatea

CSIC-UPV/EHU

Fundación Biofisica Bizkaia
Biofisika Bizkaia Fundazioa

Tesis doctoral

Development of soft and rigid membrane nanotemplates for the mechanistic analysis of Dynamin I action on curved surfaces

Unidad de Biofísica (CSIC-UPV/EHU)
Departamento de Bioquímica y Biología Molecular
Facultad de Ciencia y Tecnología
Universidad del País Vasco (UPV/EHU)

Memoria presentada por Dña Eva Rodríguez Hortelano para optar al grado de Doctor por la Universidad del País Vasco (UPV/EHU)

Directores: Dr. Vadim Frolov y Dra. Anna Shnyrova Zhadan

(c)2015 EVA RODRIGUEZ HORTELANO

PhD Thesis

Development of soft and rigid membrane nanotemplates for the mechanistic analysis of Dynamin I action on curved surfaces

by

Eva Rodríguez Hortelano

LEIOA, 2015

Cette thèse est dédiée avec toute mon affection à ma mère,

qui m'a appris que l'apprentissage est un long voyage.

Dedicado con todo mi afecto a ama,

que me enseñó que el aprendizaje es un largo viaje.

Mi madre, profesora y compañera, siempre apoyandome. Gracias por alentar mi curiosidad en la infancia y juventud, por dejarme poner la casa perdida con mis "experimentos" y desmontar todos los aparatos a pesar de que al montarlos de nuevo, siempre me sobraban piezas.

"Life isn't about finding yourself. Life is about creating yourself." — George Bernard Shaw

ACKNOWLEDGMENTS

En primer lugar, quiero agradecer a Anna y Vadim su disponibilidad y las fructiferas discusiones. Gracias por vuestro tiempo y por enseñarme a no perder la perspectiva.

Este ha sido un largo viaje lleno de aprendizaje en muchas disciplinas diferentes. Gracias a todos los compañeros que me encontré por el camino y a los que me siguen acompañando.

"And those who were seen dancing were thought to be insane

by those who could not hear the music." — Friedrich Nietzsche

A mis chicas, a todas que sois tan diferentes, sois los matices de los colores que dan viveza a la pintura, me enriqueceis como persona, gracias. A los que me ayudan a ver lo trascendente de la vida, a los que me desperezan y hacen que pueda oir la musica y ponerme a bailar, mila esker bihotz-bihotzez. Zuek bai talde bat baino askoz gehiago! A Alejandro que me saca la sonrisa sin apenas proponerselo. Gracias por ser mi apoyo incondicional, siempre confidente y siempre conmigo.

Mila esker bihotzez.

"I've learned that people will forget what you said, people will forget what you did,

but people will never forget how you made them feel." — Maya Angelou

Quiero agradecer a mi padre las noches que me llevaba a su laboratorio y me enseñaba las diferentes constelaciones, este recuerdo es uno de mis mayores tesoros.

"Hay una fuerza motriz más poderosa que el vapor, la electricidad y la energía atómica:

la voluntad humana." — Albert Einstein

PREFACE

This thesis project has been carried out in the Membrane Nano-Mechanics Group from the Biophysics Unit, Department of Biochemistry and Molecular Biology at the University of the Basque Country.

This work has been supported by the Ph.D. Fellowship program of the Biophysics Foundation.

This thesis has been partially communicated at the following International Meetings:

- SBE 2012 Spanish Biophysical Society Congress; Barcelona (Spain); Poster presentation.
- 57th Annual meeting of the Biophysical Society 2013; Philadelphia, Pennsylvania; Poster presentation.
- 58th Annual Meeting of the Biophysical Society of USA, 2014: San Francisco, California; Poster Presentation.
- SBE 2014 Spanish Biophysical Society International Congress; Alcalá de Henares (Spain); Poster presentation.

CONTENTS

ABBREVIATIONS XIII

SYMBOLS GLOSSARY...XVII

1. INTRODUCTION.. 1

1.1. Membrane curvature in cells and *in vitro*............................... 3

1.1.1. Membrane nanodomains in fusion and fission of cellular membranes.. 3

1.1.2. The classical approach to membrane curvature 5

1.1.3. Lipid NTs: flexible highly curved membrane template 8

1.1.3.1 Experimental determination of NT curvature 12

1.1.3.2 Characterization of nanoscale membrane elasticity using NT 14

1.1.4. Hemi-cylindrical arrays of rigid supported membranes with moderate curvature 18

1.2. Dynamin I: its structure and self-assembly properties 20

1.2.1. Dynamin I at a glance...21

1.2.2. .. Dynamin I self-assembly and polymerization on membrane templates 23

1.2.3. Dynamin I structure 25

1.2.4. Cooperative GTP hydrolysis by dynamin polymer 28

1.2.5. Dyn1 driven membrane fission: protein mechanics 30

1.3. Objectives 34

2. MATERIALS AND METHODS 37

2.1. Equipment and materials 39

2.1.1. GUV formation 39

2.1.2. LUV formation 40

2.1.3. SUV formation... 41

2.1.4. BLM formation... 41

2.1.5. Glass micropipettes fabrication 42

2.1.6. Micromanipulation 43

2.1.7. Optical microscopy... 43

2.1.8. Conductance measurements setup 44

2.1.9. Other equipment 45

2.1.10. Proteins 46

2.1.11. Lipids 47

2.1.12. Buffers and buffer components 47

2.1.13. Organic solvents 48

2.1.14. Nucleotides 48

2.1.15. Other materials... 49

2.1.16. Data acquisition software 49

2.1.17. Analytical software 50

2.2. Methods 51

2.2.1. Preparation of multilamellar vesicles..................................... 51

2.2.2. Formation of GUVs 52

2.2.3. Preparation of Small Unilamellar Vesicles................................55

2.2.4. Formation of LUVs 56

2.2.5. Preparation of planar bilayer lipid membranes (BLMs) 57

2.2.6. Measurements of electric conductance of NTs formed from BLMs 59

2.2.7. Preparation of supported bilayers on SiNWs 64

2.2.8. Fluorescence microscopy imaging of GUV-NT and SiNW templates 66

2.2.9. Protein dialysis..66

2.2.10. Measurements of the protein concentration 67

2.2.11. Cross-linking of the protein 67

2.2.12. Measurements of the NT constriction and fission by Dyn1.........68

3. RESULTS AND DISCUSSION.. 71

3.1. Simultaneous measurements of ionic permeability and fluorescence of NTs pulled from GUVs................................ 73

3.2. Radius and mechanical parameters of short NTs obtained from BLM 83

3.3. Quantification of membrane deformations during membrane fission mediated by Dyn1 86

3.3.1. Dyn1 P11C/Y125C Mutant 86

3.3.2. CC-Dyn1 behaviour on lipid NTs 88

3.3.3. How much force needs the Dyn1 to bend the membrane of a NT? 90

3.3.4. CxC Dyn 1 behaviour on lipid NTs 93

3.3.5. Hemifission separates two mechanistically distinct steps in fission 96

3.4. Dyn1 behavior on lipid bilayers supported on surfaced-adhered SiNW 103

4. CONCLUSIONS 107

5. BIBLIOGRAPHY 111

6. RESUMEN Y CONCLUSIONES 133

6.1. Resumen 135

6.2. Conclusiones 141

ABBREVIATIONS

AFM: Atomic Force Microscopy

AH: Amphipathic Helix

BAR: Bin-Amphiphysin-Rvs

BCA: Bicinchoninic acid

BLM: Bilayer Lipid Membrane/Black Lipid Membrane

BSA: Bovine Serum Albumin

BSE: Bundle Signalling Element

CC-Dyn1: Dynamin I with P11C & Y125C point mutations

CCP: Clathrin-Coated Pit

CHOL: Cholesterol

CME: Clathrin-Mediated Endocytosis

Cryo-TEM: Cryo Transmission Electron Microscopy

CXC-Dyn1: P11C/Y125C-Dyn1 crosslinked with MTS-4-MTS reagent

DOPC: 1,2-dioleoyl-sn-glycero-3-phosphocholine

DOPE: 1,2-dioleoyl-sn-glycero-3-phosphoethanolamine

DOPS: 1,2-dioleoyl-sn-glycero-3-phospho-L-serine

DTT: Dithiothreitol

Dyn1: Dynamin I

EDTA: Ethylenediaminetetraacetic acid

ENTH: Epsin N-terminal Homology Domain

FAPP: Four-Phosphate Adaptor Protein

FRET: Förster Resonance Energy Transfer

GBP:	Guanylate binding protein
GDP:	Guanosine-5'-diphosphate
GED:	GTPase Effector Domain
GMPPCP:	β,γ-Methyleneguanosine 5′-triphosphate
GTP:	Guanosine-5'-triphosphate
GTPγS:	slowly hydrolysable analog of GTP
GTPase:	Guanosine-5'-triphosphatase
GUV:	Giant Unilamellar Vesicle
sGUV:	Supported Giant Unilamellar Vesicles
HEPES:	4-(2-hydroxyethyl)-1-piperazineethanesulfonic acid
KCl:	Potassium Chloride
LUV:	Large Unilamellar Vesicle
MgCl$_2$:	Magnesium Chloride
MTS:	Thiol-specific homobifunctional methanethiosulfonate
NT:	Lipid membrane nanotube
NT$_{BLM}$	Lipid membrane nanotube pulled out of a Black Lipid Membrane
NT$_{GUV}$	Lipid membrane nanotube pulled out of a Giant Vesicle
PDB:	Protein Data Bank
PH:	Pleckstrin Homology
PI(4,5)P:	Phosphatidylinositol 4,5-bisphosphate
PLL:	Poly-L-Lysine
PRD:	Proline and arginine Rich Domain
PTFE:	Polytetrafluoroethylene, “Teflon”
RhDOPE:	1,2-dioleoyl-sn-glycero-3-phosphoethanolamine-N-(lissamine rhodamine B sulfonyl)
SH3:	SRC Homology 3 Domain

SiNW:	Silicon Nanowires
SUV:	Small Unilamellar Vesicle
TEM:	Transmission Electron Microscopy
WT-Dyn1:	Wild Type Dynamin I

SYMBOLS GLOSSARY

k	Bending modulus
σ	Lateral tension
r_{NT}	Radius of the NT
I_{meas}	Measured current
J	Sum of the principal curvatures
U	Applied holding potential
R_{NT}	Electrical resistance of the NT
G_{NT}	Conductance of the NT
A	Area of the transversal section of the NT
ρ	Electrical resistivity
L_{NT}	NT length
L_{NTcrit}	Critical length at which the NT forms
E_{σ}	Lateral tension energy
E_b	Bending energy
E_{Elast}	Elastic energy
I_{leak}	Part of the measured current that corresponds to the leakage
C_{sp}	Specific Capacitance
S	Area of the nanotube
k_B	Boltzmann constant
T	Temperature
F_{pull}	Force required for pulling a NT

1. INTRODUCTION

1.1. Membrane curvature in cells and *in vitro*

1.1.1. Membrane nanodomains in fusion and fission of cellular membranes

The polymorphic cellular membranes are subdivided into functional domains. In many cases the function of the domain is linked to its shape. Indeed, the majority of the cellular membrane structures are curved, with curvature varying from moderate (hundreds nm in tubular organelles and trafficking carriers) to extreme (few nm for fission/fusion pores) values. In the last decade it has been recognized that membrane curvature plays a crucial role in the self-organization and function of membrane domains. *In vitro* experiments directly showed that membrane curvature can drive segregation of membrane components into distinct membrane domains (McMahon and Gallop, 2005). *In vivo* experiments further confirmed that induction of membrane curvature could trigger a cascade of membrane transformations resulting in formation of a new membrane compartment (Renard et al., 2015; Sorre et al., 2009).

The curvature effects become even more evident in the case of extremely confined and curved membrane domains involved in fusion and fission of cellular membranes. Both processes are highly localized to small membrane sites where membrane remodeling is carefully organized by specialized proteins (Frolov et al., 2014). It is generally accepted that membrane fusion and fission proceed through similar set of membrane rearrangements, involving creation of highly curved membrane intermediates, hourglass membrane necks and non-bilayer stalk-type transmembrane bridges (Chernomordik and Kozlov, 2003; Frolov et al., 2014). These structures are characterized by extreme curvatures (1/10-1/2 nm^{-1}) with generally well-defined protein composition. Thus, the differences in curvature and composition make this kind of sites distinct membrane domains.

The small size and transient nature of such domains complicates their properties study. Thus, fundamental mechanical parameters of these nanoscale domains as well as dynamics and energetics of protein interactions with such domains remain poorly characterized. This is the reason why novel experimental techniques are needed to obtain quantitative information about structure and function of membrane nanodomains (Arumugam and Bassereau, 2015). The main goal of this PhD thesis was the development of new experimental approaches for studying nanomechanics of highly curved membrane domains. The specific focus was on development of new membrane templates suitable for studying curvature driven processes with high spatial and temporal resolution.

Membrane templates mimicking the geometry of specific cellular membrane organelles are widely used for *in vitro* reconstitution of membrane processes. These templates may be classified into two main categories: a) the soft (e.g. membrane vesicles or nanotubes) and b) the rigid templates (self-assembled or supported by a rigid artificial nanotemplate). Reconstitution of cellular processes on such templates helped revealing fundamental mechanism of curvature sorting, membrane mechanics (including curvature creation), etc. However, the available membrane templates rarely approach the curvatures characteristic for membrane remodeling. Below we review the main approaches and discuss their applicability to the study of fusion and fission nanodomains.

1.1.2. The classical approach to membrane curvature

Large and small unilamellar membrane vesicles (LUVs and SUVs) with diameters ranging from hundreds to tens of nm were the original templates of choice for *in vitro* reconstitution of membrane processes associated with high curvature. Assays such as gradient separation or pull down assays have been instrumental to measure the preferential association of proteins to membranes of certain curvature (Busse et al., 2013; Chung et al., 2008). Recently, arrays of vesicles attached to a planar support have been successfully used to characterize protein interaction with individual vesicles using quantitative fluorescence microscopy (Christensen and Stamou, 2010). This approach allows real time monitoring of the protein adsorption on vesicles of different sizes. Transmission electron microscopy (TEM) and cryo-TEM are generally used to resolve nanoscale deformations of vesicles caused by adsorbing proteins (Mears and Hinshaw, 2008; Varkey et al., 2010). Thanks to these methods main modes of curvature creation in cellular membranes (curvature scaffolding and membrane insertion) have been identified (McMahon and Gallop, 2005; Zimmerberg and Kozlov, 2006). Furthermore, specialized protein domains utilizing local scaffolding (e.g. crescent-shapes BAR domains (Gallop and McMahon, 2005; Itoh and De Camilli, 2006; Mim and Unger, 2012)) and insertion (ENTH, amphipathic helices (Itoh and De Camilli, 2006)) have been characterized. Interestingly, addition of such proteins to spherical vesicles triggers the so-called membrane tubulation: transformation of vesicles into highly curved membrane cylinders covered by the proteins (Itoh and De Camilli, 2006). The equilibrium radius of such cylinders characterizes the curvature activity of protein species: creation of extremely high curvatures (1/10 nm^{-1}) have been documented for proteins involved in membrane fusion and fission, identifying the local protein-driven membrane stress as the main driving force for membrane remodeling in cells (Kozlov et al., 2010). Vesicle deformations induced by external forces (such as osmotic pressure) or by addition of membrane-inserting molecules, proteins and lipids, were also used to extract mechanical parameters of the vesicle membrane through the analysis of vesicle shape diagrams (Frolov et al., 2011; Mui et al., 1995).

In general, the combination of biochemical and morphological characterization of vesicular templates remains instrumental in revealing the mechanisms of action of key cellular players and allows identifying specialized protein domains. However, it analyzes only stationary membrane shapes and is not suitable for studying dynamics of membrane remodeling, with associated transient membrane intermediates and force factors.

An additional disadvantage for studying fusion/fission by using the vesicle-based systems is that their curvature usually remains moderate (1/100 nm^{-1}). Galactosylceramide nanotubes (Kulkarni et al., 1995; Stowell et al., 1999) are an exception to this rule as this system was the first one that allowed mimicking the highly curved membrane necks characteristic for membrane fusion/fission. These nanotubes are used to analyzed protein binding and self-assembly on extremely curved membrane surfaces (Stowell et al., 1999). However, the geometry and composition of these nanotubes allows only for small variations, severely limiting the range of real applications.

1.1.3. Lipid NTs: flexible highly curved membrane template

Generation of high membrane curvature templates that can be dynamically controlled independently on membrane composition was possible with lipid membrane nanotubes (NTs) pulled from a reservoir. Such NTs remains the common template for studying membrane processes at high curvature (Bashkirov, 2006; Jesorka and Orwar, 2009; Roux et al., 2005; Shnyrova et al., 2013; Svetina and Zeks, 2014). The NT is a membrane cylinder "pulled" from a parent membrane by a local force (Roux, 2013) (Figure 1.1.). The "pulling" experiments are dated back to 1973, when an NT was produced from a red blood cell membrane using shear flow (Hochmuth et al., 1973). That experiment allowed obtaining the stretching modulus of the lipid bilayer and the NTs were further used to characterize the visco-elastic behavior of lipid bilayers (Heinrich et al., 1999; kwok, 1981; Waugh, 1979) and cellular membranes (Dai and Sheetz, 1995; Raucher and Sheetz, 1999; Waugh, 1982)). Measurements of the force required for pulling an NT from cellular membranes also report effective lateral tension of the membrane, linked to membrane adhesion to cytoskeleton (Raucher and Sheetz, 1999). Recently, the NTs were also used to understand the role of curvature in compositional demixing and formation of membrane domains (Callan-Jones et al., 2011; Heinrich et al., 2010; Sorre et al., 2009).

As mentioned above, the NTs are formed through applying a “point” force to a reservoir (parent) membrane. The pathway of NT formation is depicted in Figure 1.1.

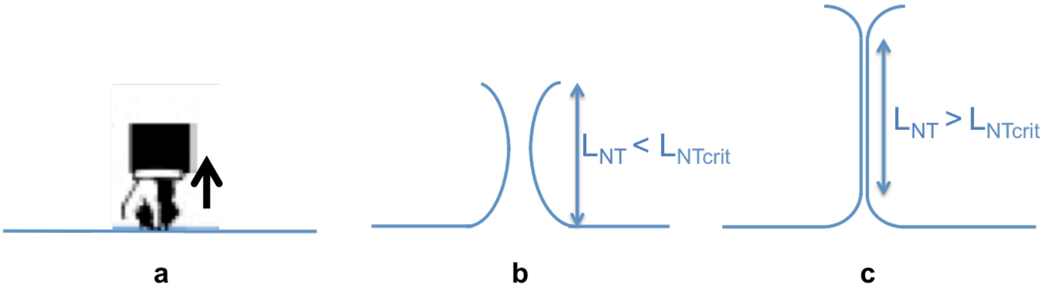

Figure 1.1. Schematic representation of a NT formation. a) NT can be pulled from the flat membrane of a bilayer lipid membrane (BLM) or giant unilamellar vesicle (GUV). The pulling force may be applied by a glass micropipette attached to a piezo-manipulator (Bashkirov et al., 2008), optical tweezes (Bar-Ziv et al., 1998), magnetic tweezers (Hosu et al., 2007) or shear flow (Pucadyil and Schmid, 2010). b) Upon enough pulling force is applied, the membrane starts its deformation adopting a catenoid shape, the minimal surface configuration for small NT (Frolov et al., 2003). c) By pulling from the NT end further up, a critical length (L_{NTcrit}) is reached. At this point, the system reaches new energy equilibrium and the catenoid collapses. From now on the NT acquires its cylindrical shape.

First, the short membrane neck forms, its shape described by a catenoid ((Roux, 2013), Figure 1.1. b). Upon reaching certain critical length, the catenoid connection is transformed into a cylindrical nanotube (Frolov et al., 2003; Powers et al., 2002) (Figure 1.1. c). The catenoid-cylinder transition corresponds to the pulling force "overshoot" (Campillo et al., 2013; Koster et al., 2005; Roux, 2013). The force increases with catenoid length (tens of pN dependently on membrane tension (Koster et al., 2005)) and then drops to a constant level (few pN) defined by the radius of the cylinder. The force does not depend on the cylinder length (Koster et al., 2005; Roux, 2013), hence the radius of the cylinder reports the mechanical parameters of the parent membrane: its bending rigidity (k) characterizing the curvature elasticity of the membrane and the lateral tension (σ), characterizing the work against membrane reservoir. In the simplest approximation, these two terms fully describe the elastic part of the free energy of the NT (Deserno, 2014):

$$E_{elast} = \sigma \, \Delta S + \int_S \frac{k}{2} J^2 \, dS \qquad \text{(Eq. 1.1)}$$

where J is the sum of the principal curvatures of the membrane surface (here equal to $1/r_{NT}$, being r_{NT} the radius of the cylindrical NT) and $\Delta S = 2\,\pi\, r_{NT}\, L_{NT}$ (L_{NT} is the NT length) is the NT area. The minimization of E_{elast} as a function of r_{NT} yields:

$$r_{NT} = \sqrt{\frac{k}{2\,\sigma}} \qquad \text{(Eq. 1.2)}$$

The bending rigidity of a membrane is generally a weak function of its lipid composition (varying from 10 to 30 k_BT for physiologically-relevant membrane compositions). Thus, by controlling lateral tension of the reservoir one can manipulate the NT geometry (Figure 1.2).

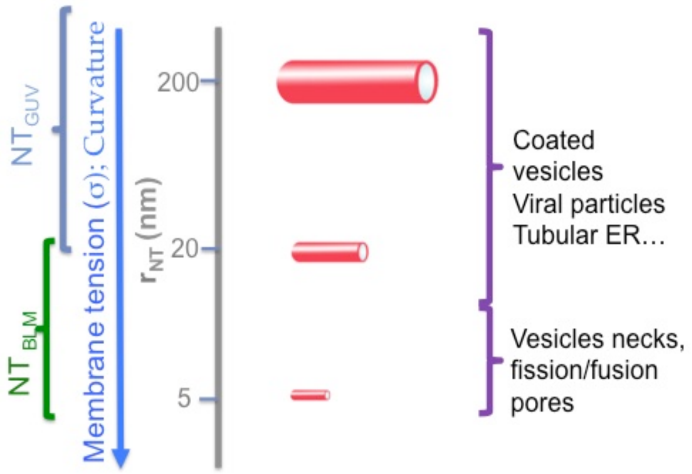
NT GUV
NT BLM
Membrane tension (σ); Curvature
r NT (nm)
200
20
5
Coated vesicles
Viral particles
Tubular ER…
Vesicles necks, fission/fusion pores

Figure 1.2. The NT curvatures cover the whole range of cell membrane curvatures. As the radius of the NT is set by the tension of the mother membrane, by pulling NTs form membrane templates with different tension, such as the BLMs and GUVs, we may obtain NTs with different radii values.

In reverse, the mechanical parameters (bending rigidity and lateral tension) of the substrate lipid membrane can be obtained via force measurements on lipid NTs. Moreover, if one of the parameters is known, the NT radius can be measured and thus the geometry of the NT can be characterized.

1.1.3.1 Experimental determination of NT curvature

The typical range of NT radii are from tens to just few nanometers (Figure 1.2.), i.e. they are located near or below the diffraction limit of optical microscopy. This makes it challenging to measure the NT radius directly, and explains the need for quantitative and complementary techniques (Adams et al., 2010; Stepanyants et al., 2012). The basic method for characterization of geometry of NTs pulled from GUVs consists in the measurement of area decrease of the GUV as function of the NT length (Henriksen and Ipsen, 2004). This method requires very long NTs to produce measurable changes in GUV projected area. Alternatively, the NT radius can be obtained from the pulling force measurements (e.g. via optical or magnetic tweezers (Roux, 2013)), providing that the lateral tension of the parent membrane is known or controlled. In GUV experiments, the tension can be controlled by applying the so-called micropipette aspiration method (Tian et al., 2009), where the GUV is partially sucked into a tens of micron glass pipette using precisely controlled pressure. The NT radius is then recalculated using $\mathrm{F}_{pull} = 2\,\pi\, r_{NT}\, \sigma$ formula for stationary cylindrical NTs (Koster et al., 2005; Roux, 2013). As the method requires an *a priori* knowledge of lateral tension of the parent membrane it cannot be directly applied to free-standing membranes, such as cellular membranes.

The technique that our group has developed in the recent years to access the geometry of lipid NT is based upon the measurements of the ionic permeability of the NT lumen using voltage-clamp technique (Neher, 1976). Consider a hollow cylindrical NT filled with an ionic solution. By applying a potential difference between the NT ends and measuring the electrical current at fixed potential difference, we can then recalculate the NT conductance by using Ohms law as follows:

$$I_{meas} = \frac{U}{R_{NT}} = U \cdot G_{NT} \qquad \text{(Eq. 1.3)}$$

where, I_{meas} is the measured current, U is the applied holding potential, the R_{NT} is the electrical resistance of the NT lumen and finally the G_{NT} is the conductance of the NT. At physiological ionic strength the Debye screening length (below which one needs to introduce corrections to the Ohms law) is ~ 1 nm, hence for most of NTs we can calculate the NT conductance as:

$$G_{NT} = \frac{A}{\rho\, L_{NT}} = \frac{\pi\, r_{NT}^2}{\rho\, L_{NT}} \qquad \text{(Eq. 1.4)}$$

where, A is the transversal section of the NT lumen and ρ is specific resistance of the electrolyte solution. Thus, for an NT with a known length, the NT conductance reports the NT radius. Accordingly, changes in the conductance (at fixed L_{NT}) indicate the shape transformations of the NT, its expansion or constriction. The technique allows us measuring the changes in the NT radius with high spatial (0.5 nm) and temporal (0.5 ms) resolution (Supplementary information in Shnyrova et al., Science 2013). However, if the NT shape deviates from a cylinder, complementary information will be needed in order to interpret the changes in the NT conductance and relate them to the NT shape (see below, "Simultaneous fluorescence and conductance measurements" in the Results section).

1.1.3.2 Characterization of nanoscale membrane elasticity using NT

Even smallest membrane domains representing sites of membrane fusion and fission contain hundred of lipid molecules. Their deformations then can be described in terms of thin shell elasticity and corresponding elastic moduli. In the simplest approximation of small membrane deformations with fixed topology (see Eq. 1.1. (Evans, 1987)), the mean curvature bending modulus k is the main parameter determining the energetics of the deformations at nanoscale. The bending modulus is affected by external parameters, such as temperature, solutes and, importantly, membrane composition (Cantor, 1999; Marsh, 2006). Hence it becomes imperative to directly measure the modulus for each particular membrane system/composition.

There are a large number of experimental techniques elaborated to measure the bending modulus. We can distinguish "non-invasive" methods based upon analysis of intrinsic behavior of a membrane and the methods analyzing the membrane deformations produced by an external force.

The non-invasive methods generally analyze temperature-driven fluctuations of a membrane shape at a stationary membrane configuration. They are generally applied to "soft", low curvature membranes, such as GUVs (synthetic and cell-derived (Dobereiner et al., 2003; Henriksen and Ipsen, 2002)) or freely suspended lipid bilayers (Liu and Nagle, 2004), as well as to cellular plasma membrane (Zilker et al., 1992). As the amplitude of the fluctuation is reversely proportional to bending stiffness, the analysis of the amplitude distribution at a given temperature yields the bending modulus of the membrane (Olbrich et al., 2000). The shape fluctuations are analyzed either directly, via obtaining a sequence of images by fluorescence or phase-contrast microscopy (Baumgart et al., 2003), or indirectly, via reflectivity measurements (Liu and Nagle, 2004). The method operates at large length scale and yields "bulk" (averaged over possible fluctuations of composition, localized non-linearities, etc.) elastic moduli.

Large-scale membrane deformations can also be produced by external force, such as electric field (Serral, 2010). Application of alternating electric field to a GUV induces bulk deformations linked to dielectrophoretic forces (Korlach et al., 2005). The elliptical shapes adopted by the vesicle are further analyzed to relate the power of the electric field to the deformation amplitude and thus extract the membrane elastic constants. Electric field can also produce a focal force pulling cylindrical membrane structures from cellular membranes (Kozlov et al., 1992). Similar membrane deformations can be achieved through different local (often termed "point") pulling forces. As described earlier, membrane nanotubes produced by such forces have become a universal tool for analysis of membrane mechanics at nanoscale and investigation of curvature effects on membrane processes (Roux, 2013; Singh et al., 2012). Furthermore, the nanotube system allows for "scaling down" the system dimensions via creation of extremely short (100 nm length) and curved (5 nm radius) NTs mimicking cellular nanodomains (Bashkirov et al., 2008; Shnyrova et al., 2013). Even smaller length scales can be achieved by using Atomic Force Microscopy (AFM), which allows to directly measure the elastic response from a small membrane patch (Steltenkamp et al., 2006). The main pitfall of this technique, however, is the direct (contact) way of the force application that interferes with membrane processes due to steric hindrance.

Summarizing, the nanotube pulling remains the technique of choice for studying changes of membrane elasticity at nanoscale. But, how is the bending rigidity measured in this technique? As we described above (Eq. 1.1.), the nanotube radius is determined through known lateral tension and bending rigidity. Knowing radius and tension (or, equivalently, the pulling force), one can recalculate k (see Eq. 1.2.). Micromanipulations on NTs under conditions of controlled pulling force and lateral tension have become a powerful tool in studying membrane mechanics and proteo-lipid interactions (Heinrich et al., 2010; Roux, 2013; Roux et al., 2005; Singh et al., 2012). Bending rigidity (k) of various lipid species and their mixtures, including phase-separating mixtures, has been measured (Tian et al., 2009). Furthermore, changes in membrane elasticity induced by protein adsorption onto the NT membrane have been characterized (Sorre et al., 2009). Yet in most of these techniques the measurements have been done using microns-long NTs, making the study of activity of individual protein complexes operating at nanoscale a challenge for these techniques.

Completely different approach to k measurements is used in the conductance measurements experiments (detailed explanation to NT conductance measurements is given in the Methods chapter below). To access membrane tension it was proposed earlier to analyze the radius dependence on the voltage driving the current through the nanotube (Bashkirov, 2006). This method would allow real-time measurements of k without an *a priori* knowledge on membrane tension of the parent membrane. Hence it could be applied to different membrane systems and in situations when the tension changes in the course of the experiment (e.g.

due to protein adsorption). Furthermore, this technique provides a unique possibility to resolve dynamics of nanoscale membrane transformations. The spatial resolution of this method depends on the geometry of the nanotube. For short submicron NTs, slightest membrane deformations result in detectable changes in the NT conductance, so that curvature activity of individual proteins and small protein complexes can be resolved in real time (e.g. Shnyrova et al, 2013).

One of the main goals of this work is to improve this methodology and further apply it to nanotube templates used for studying nanoscale membrane deformations produced by dynamin 1 (Dyn1).

1.1.4. Hemi-cylindrical arrays of rigid supported membranes with moderate curvature

While soft membrane templates are intended to mimic physiological situations and reconstitute curvature activity of the proteins, the rigid ones can reveal how membrane curvature affects protein action. Recent advances in nanotechnology make possible fabrication of various nano-templates that can be suitable as supporting surfaces for lipid membranes. Supported lipid bilayers follow the curvature patterns when grafted to such surfaces. An example of such a nanofabricated template is a wavy glass surface used for creation of periodic patterns of supported membrane curvature approaching 0.01 nm^{-1} at the peaks (Hsieh et al., 2012). Here, the membrane curvature gradients resulted in clear demixing of membrane components seen by fluorescence microscopy (Hsieh et al., 2012). Another example of a curved nano-template attractive for lipid bilayer are the silicon nanowires (SiNWs). The SiNWs are cylindrical wires with 10s of nm in diameter and variable length. Diameter of the SiNW can be controlled with a 2-5 nm precision. The SiNW can be attached to a flat surface creating a platform for microscopic characterization of the protein interaction with the SiNW-supported lipid bilayer. Recently, such supported bilayers were used to reconstitute transport activity of transmembrane proteins (Tunuguntla et al., 2015). Unlike wavy glass, these templates provide hemi-cylindrical geometry with large (equivalent to a hemi-cylinder (Tunuguntla et al., 2015) area of constant curvature, more relevant for tubular/cylindrical geometry of membrane remodeling in fusion and fission. In this work, we adapted these templates for studying curvature-dependent membrane interactions of Dyn1.

1.2. Dynamin I: its structure and self-assembly properties

In this work we have focused on the protein Dynamin 1 (Dyn1), the GTPase controlling membrane fission in endocytosis in neurons. Dyn1 is one of the most characterized proteins involved in membrane remodeling in cells (Ferguson and De Camilli, 2012). The structures of both, individual dynamin molecule and dynamin oligomers implicated in membrane fission were resolved (Faelber et al., 2011; Ford et al., 2011). Dyn1 remains active *in vitro*: purified Dyn1 is capable to create high membrane curvature and produce fission of pure lipid bilayers (Roux et al., 2006; Sweitzer and Hinshaw, 1998). The structural information is also available for intermediate conformations of Dyn1 in complex with different GTP analogues (Faelber et al., 2012; Faelber et al., 2011; Ford et al., 2011). This information is critical for relating the protein structure to membrane deformations linked to progression of GTPase cycle of Dyn1. Thus, Dyn1 seems to be the protein of choice for studying the nanomechanics of membrane remodeling.

1.2.1. Dynamin I at a glance

Dyn1 was first identified by Shpetner and Vallee in 1989 while trying to isolate new microtubule based motors from the bovine brain (Shpetner and Vallee, 1989). This protein becomes the first member of what is now known as “dynamin superfamily”, the family of large Guanosine-5’-Triphosphate (GTP) phosphohydrolases (GTPases) which includes classical dynamins, dynamin-like proteins, Mx proteins, OPA, mitofusins, and guanylate binding proteins (GBPs) (reviewed in (Danino and Hinshaw, 2001; McNiven et al., 2000; Praefcke and McMahon, 2004; van der Bliek, 1999). The first indications of dynamin involvement in membrane remodeling during synaptic transmission emerged in late 80s in studies of the temperature-sensitive dynamin homolog *shibire* in Drosophila flies (Koenig and Ikeda, 1989). Upon shifting to non-permissive temperatures (Grigliatti et al., 1973), rapid paralysis of the *shibire* flies was observed. Ultra-structural analysis of the presynaptic nerve terminals of these flies revealed depletion of synaptic vesicles and accumulation of omega-shaped membrane profiles corresponding to the clathrin coated pits (CCPs) that remained attached to the plasma membrane. Single or double electron-dense bands, or collars encircled the necks of these membrane invaginations. In 1995 Takei and co-authors treated permeabilized rat synaptosomes with the non-hydrolyzable analog of GTP, the GTPγS (Takei et al., 1995). What they observed were long membrane invaginations coated with clathrin on their dome and decorated with multiple electron dense collars. Binding of antibodies recognizing Dyn1 to the long collars confirmed that they are covered by dynamin.

Since these initial observations it has become gradually understood that Dyn1 is involved at different stages of clathrin-mediated endocytosis (CME) (Mettlen et al., 2009; Nunez et al., 2011). Formation of endocytic vesicles can be briefly described as follows. As a clathrin-coated pit (CCP) emerges, clathrin molecules and its adaptor proteins produce an invagination of the plasma membrane (Heuser and Anderson, 1989). At this stage Dyn1 plays a regulatory role: in combination with clathrin and actin it creates specific checkpoints to control the vesicle maturation (Mettlen et al., 2009; Nunez et al., 2011). Once the CCP matures and acquires its spherical shape, its connection with the plasma membrane becomes a narrow membrane neck. Dyn1 is targeted to the highly curved neck and forms the protein collars around it. Dyn1 polymerization triggers cooperative GTP hydrolysis causing fission of the neck and disassembly of the dynamin collar (Mettlen et al., 2009) (Figure 1.3.). The mechanism of fission has attracted the attention of many researchers during the last decades (Ferguson and De Camilli, 2012) and is currently related to cooperative conformational changes in dynamin polymer, driven by GTP hydrolysis.

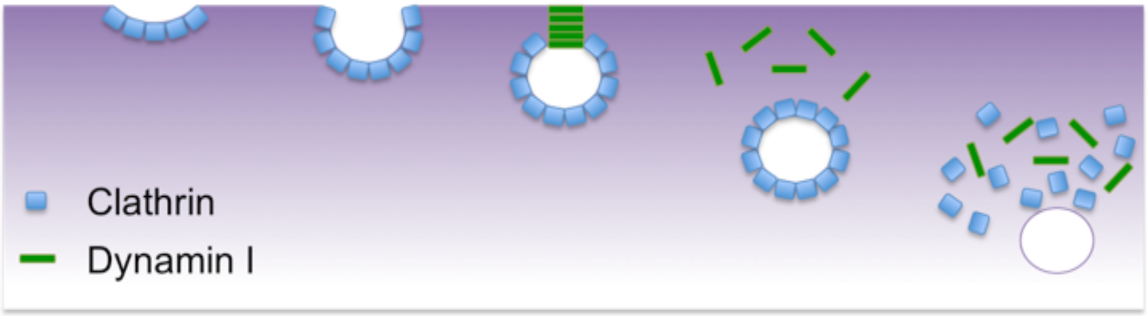

Figure 1.3. Schematic representation of the CME. The membrane curvature is created by clathrin (blue) in cooperation with adaptor proteins assembling a dense protein layer on the plasma membrane. Polymerization of clathrin into a spherical cage results in formation of the vesicle connected to the plasma membrane by a thin neck. Dynamin (green) is attracted to the high curvature of the neck and polymerizes into a scaffold around it. Upon GTP hydrolysis, the neck undergoes fission and dynamin scaffold is disassembled.

1.2.2. Dynamin I self-assembly and polymerization on membrane templates

One of the key characteristics of Dyn1 is its ability to polymerize on a curved membrane surface. *In vivo*, under constant presence of GTP, the polymerization competes with the depolymerization process driven by GTP hydrolysis, so that only short, self-limited dynamin oligomers form (Schmid and Frolov, 2011). This kinetic competition limits the size of Dyn1 collars forming on the necks of endocytic vesicles (Figure 1.4.c). These short collars apparently mediate the fission: the appearance of longer structures has only be detected when the fission is inhibited, e.g. via impairment of the Dyn1 ability to hydrolyze GTP (Takei et al., 1995). Similar long structures were detected *in vitro* when purified Dyn1 alone was added to lipid templates. In the absence of nucleotide Dyn1 induces membrane tubulation: production of narrow membrane tubules densely covered by the protein (Figure 1.4. a,b) (Carr and Hinshaw, 1997; Faelber et al., 2012; Faelber et al., 2011; Ford et al., 2011; Hinshaw and Schmid, 1995).

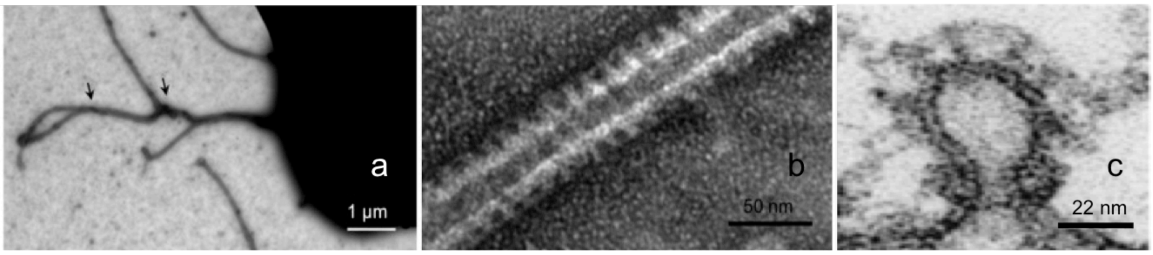

Figure 1.4. Short versus long Dyn1 scaffolds. a) Dyn1 originates tubulation of flat membranes as observed by negative staining electron microscopy. A Tubulation of SUPER template is seen (Pucadyil and Schmid, 2008). Scale bar 1 µm. b) One of the tubules from *a* at higher resolution (Pucadyil and Schmid, 2008). Bar 50 nm. c) Thin section micrograph of a CCP in drosophila shibire nervous termini (Takei et al., 1995). Bar 22 nm.

These tubules were instrumental in the structural analysis of Dyn1 polymerization. Analysis of cryo-electron microscopy images of the tubules revealed that Dyn1 forms regular helices with 12-13 nm pitch and internal diameter of 11 nm, thus imposing dramatic membrane constriction (Zhang and Hinshaw, 2001). The electron density maps obtained from the analysis of multiple helices were further used to fit in the crystallographic structure of dynamin and/or its domains. As the result a comprehensive picture of interactions between different domains of Dyn1 was reconstructed (Chappie et al., 2011).

1.2.3. Dynamin I structure

Dyn1 is a multidomain protein containing 5 distinct domains in its tertiary structure (Figure 1.5.a) (van der Bliek, 1999):

1 **G domain:** large amino-terminal GTPase domain, which is responsible for GTP hydrolysis.

2 **Middle domain:** contained in the “stalk” region of the protein is involved in the self-assembly of the protein.

3 **GTPase Effector Domain (GED):** it is also contained within the “stalk” and involved in the self-assembly, however it has been found that the self-assembly of Dyn1 stimulates its GTPase activity via this domain (Warnock et al., 1996).

4 **Pleckstrin Homology (PH) domain**: domain responsible for the interaction of Dyn1 with lipid membranes, and especially with phosphoinositides (Ramachandran et al., 2009; Salim et al., 1996).

5 **Proline and arginine Rich Domain (PRD)**: carboxyl-terminal domain that is responsible for the binding of Dyn1 to the SH3 domains of clathrin adaptors. This domain is not essential for GTP hydrolysis or polymerization of Dyn1 *in vitro*. Indeed the absence of the PRD results in more compressed and strongly packed spirals of Dyn1 than that observed with wild type Dyn1 (Carr and Hinshaw, 1997). As a consequence, for *in vitro* experiments the ΔPRD form of Dyn1 is commonly used.

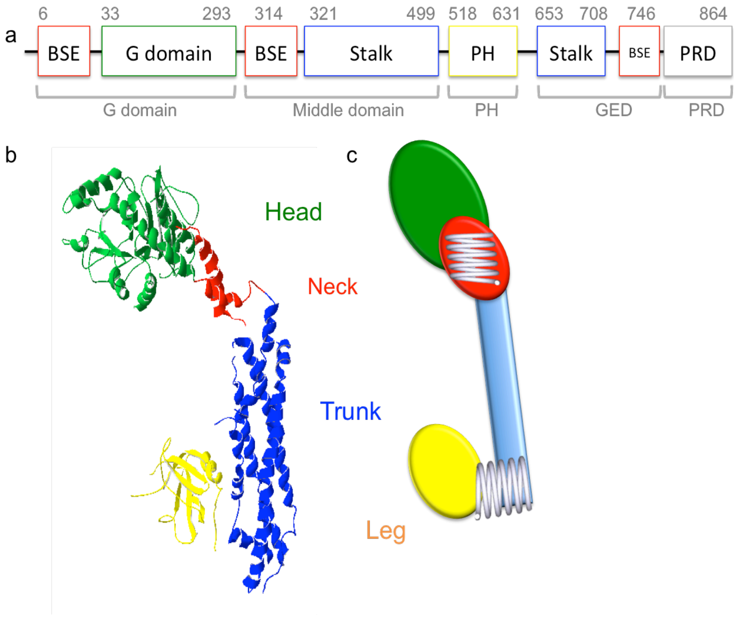
a
6
33
293
314
321
499
518
631
653
708
746
864
BSE
G domain
BSE
Stalk
PH
Stalk
BSE
PRD
G domain
Middle domain
PH
GED
PRD
b
c
Head
Neck
Trunk
Leg

Figure 1.5. Dyn1 structure. a) The domains of the protein. b) Crystal structure of Dynamin I monomer. (PDB file from: (Chappie et al., 2011)). c) Schematic representation of the folded protein showing its head, neck, trunk and leg. Spirals indicate intrinsic flexibility.

Upon protein folding the domains interact forming 4 distinct parts termed head (the upper, more distant from membrane part of the protein formed by its G domain), neck formed by three helixes from GED, middle and

G domains (also termed the bundle signaling element (BSE)), trunk or stalk, and the leg (Figure 1.5. b, c) (Low and Lowe, 2010). In 2011, two groups were able to obtain the high-resolution crystal structure of the whole molecule of Dyn1 in the absence of nucleotide (Faelber et al., 2011; Ford et al., 2011).

Being a monomer in solution at high ionic strength (Warnock et al., 1996), at physiological ionic strength Dyn1 is mostly tetrameric (Gao et al., 2010; Muhlberg et al., 1997). However, its oligomeric structure changes dramatically in the presence of a membrane: it forms a helical polymer that imposes cylindrical geometry on the encaged lipid bilayer (Figure 1.6.). Formation of the helix, driven by evolutionary-conserved interactions between different dynamin domains (Faelber et al., 2011), produces energy required for membrane tubulation (Roux et al., 2010). Polymerization is also required for two important geometrical arrangements. First, it puts G domains in the neighbouring rungs of the helix in a position promoting G-G dimerization required for GTP hydrolysis (see below, Figure 1.7). Second, it aligns the PH domains of Dyn1 so that they form ring-like membrane wedges producing local deformations facilitating membrane fission.

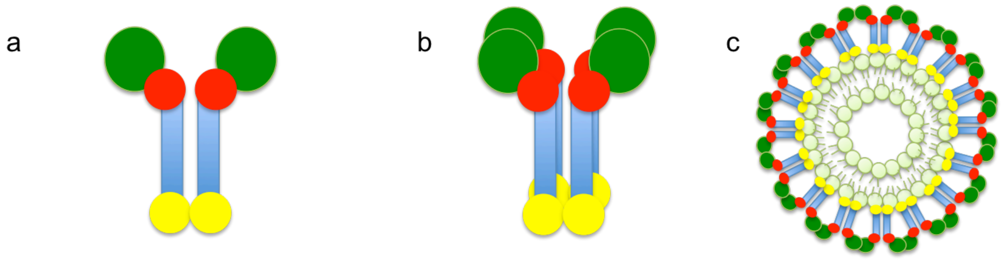

Figure 1.6. Different polymerization states of Dyn1. a) Dyn1 dimer. The head is shown in green, the neck in red, the trunk is in blue and the leg is in yellow. b) In solution Dyn1 is mostly a tetramer. c) Dyn1 polymerizes into a spiral-like structure around membrane necks.

1.2.4. Cooperative GTP hydrolysis by dynamin polymer

GTP hydrolysis is a catalytic reaction, where the GTPase form a catalytic center that facilitate severing of the phosphate bond and help utilizing the energy of the phosphate release. The GTPase activity of Dyn1 is maximized in the polymerized state of Dyn1 (Figure 1.7). Interaction between G domains in the neighbor rungs of the helix triggers G-G dimerization. The dimerization optimizes the structure of the catalytic center, resulting in ~100times increase of the rate of GTP hydrolysis, as compared to GTP hydrolysis by Dyn1 in solution (Chappie et al., 2010).

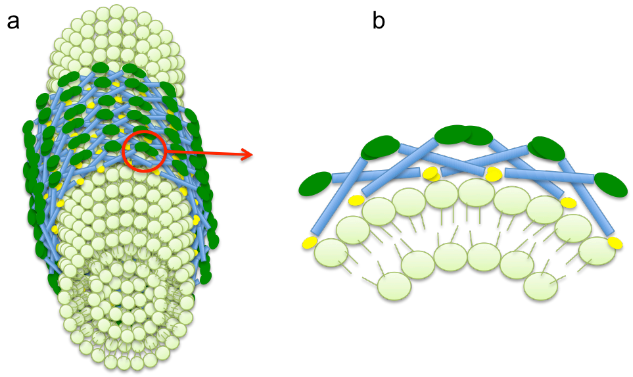

Figure 1.7. Polymerization of Dyn1 promotes G-G domain dimerization. The polymerization of a Dyn1 spiral around a membrane neck shown in a, allows for the proximity of the G domains of adjacent Dyn1 molecules in the spiral (shown in b), thus optimizing the G domain conformation for GTP hydrolysis.

The hydrolysis cycle is depicted in figure 1.8. Tight GTP binding to the G-G-dimer (ground state) triggers the hydrolysis reaction that proceeds through the transition state to the product release. The release of GDP and phosphate is coupled to disassembly of Dyn1 polymer by a yet unknown mechanism (Ramachandran et al., 2007; Schmid and Frolov, 2011). The cycle will start again with *de novo* assembly of a new Dyn1 helix. Importantly, the hydrolysis can be specifically arrested at different stages using the nucleotide analogues: addition of GMPPCP stabilizes the ground state while addition of GDP and AlF_4 results in a stable transition-state mimicking condition. Polymerization of Dyn1 in the presence of these nucleotides was analyzed by cryo-EM to reconstruct the conformational rearrangements of Dyn1 helices in the process of GTP hydrolysis.

Figure 1.8. General GTPase cycle. The cycle starts with ground state upon GTP binding to the enzyme (corresponding to the G-G dimerization of Dyn1). In the transition state or the state with the maximal energy there is a conformational change in Dyn1 molecule. Finally, there is a phosphate release followed by the inactivation of the GTPase.

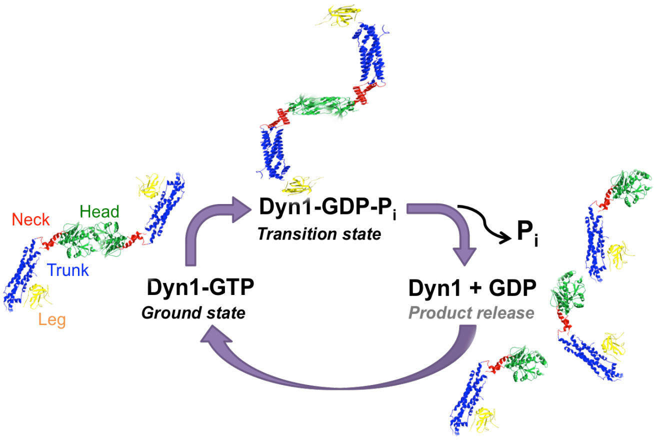
Neck
Head
Trunk
Leg
Dyn1-GDP-P_i
Transition state
P_i
Dyn1-GTP
Ground state
Dyn1 + GDP
Product release

1.2.5. Dyn1 driven membrane fission: protein mechanics

Truncation of PRD domain of Dyn1 facilitates its self-assembly, both in solution and on a curved membrane surface (Zhang and Hinshaw, 2001). Analysis of ΔPRD helices obtained in the presence of GMPPCP (ground state) and in the absence of nucleotide revealed dramatic decrease of the luminal diameter of the helix (from 11 to ~5 nm), indicating that the membrane constriction by Dyn1 is directly coupled to the its GTPase activity. The electron density maps obtained from the helix stabilized in the ground state was further used for mapping of conformational rearrangements of Dyn1 molecule. The structure of the whole Dyn1 in the presence of nucleotide is yet to be obtained. However, the structures of the head region including G-G dimer and BSE bound to GMPPCP and GDP-AlF_4 were recently identified (Chappie et al., 2011).

They revealed a surprisingly large movement in the BSE that goes from an "open" configuration in the ground (GMPPCP-bound) state (Phillips et al., 2008) to a "closed" configuration in the transition (AlF_4^-GDP-bound) state (Figure 1.9.). GDP-AlF_4 structure does not fit into the GMPPCP helix map, suggesting further decrease of the luminal diameter of the helix during the progression from ground to transition state (Chappie et al., 2011).

Daumke group further analyzed theoretically the possible long-range changes in dynamin polymer produced by the BSE movement (Faelber et al., 2011). They found several possible outcomes: 1) membrane constriction, 2) popp-ase and 3) twistase activity. Those modes of action have been already proposed earlier (Sever et al., 2000; Song and Schmid, 2003), but now there is a structural basis behind them. So following we will discuss this models in more details.

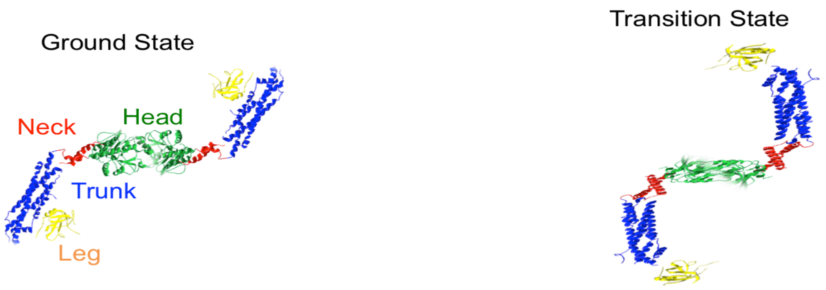

Figure 1.9. The BSE movement during evolution from the ground to the transition state has big consequences for the overall G-G dimer structure of Dyn1 (Chappie et al., 2011).

1) **Constrictase:** The model assumes that the energy of GTP binding and hydrolysis is transformed into membrane constriction driven by progressive narrowing of the lumen of Dyn1 helix (Hinshaw and Schmid, 1995). Two main mechanisms of the energy transduction have been proposed. The power-stroke model assumes that cooperative GTP hydrolysis results in acute membrane constriction due to changes in the geometry of the whole Dyn1 (Chappie et al., 2011). The ratcheting model assumes that the GTP hydrolysis fuels processive constriction where Dyn1 helix acts as a garrote (Cocucci et al., 2014; Morlot et al., 2012).

2) **Poppase:** Here, the GTP hydrolysis triggers changes of the pitch of the dynamin spiral (Stowell et al., 1999), producing both additional constriction (Kozlov, 1999) and an axial force.

3) **Twistase (either power-stroke or ratcheting):** This model, related to the constrictase model, proposes that the processive constriction of the helix also results in torque/friction forces contributing to membrane destabilization (Morlot et al., 2012).

4) **Let-go stochastic model:** Principally different from the models above, this model assumes that the energy of GTP hydrolysis is used not for constriction of the membrane but for disassembly of Dyn1 scaffold (Bashkirov et al., 2008; Sundborger et al., 2014), coupled to creation of catalytic pathway for membrane fission (Schmid and Frolov, 2011; Shnyrova et al., 2013).

How to distinguish between these models? The pathway we follow is reconstitution of individual steps of the reaction via protein engineering (targeting short-living transition states of Dyn1) and creation of specialized membrane nanotemplates. In our group we have developed such templates – the short soft lipid nanotubes - allowing us for the first time to resolve the activity of individual fission machinery constituted by 2 Dyn1 rings (Shnyrova et al, 2013). In the present work we intended **to further develop these experimental techniques and implement them to quantify the mechanical action of Dyn1.**

1.3. Objectives

- Quantify the membrane constriction activity of Dyn1 using highly curved soft membrane NTs.
  - Develop experimental protocols for simultaneous monitoring of the ionic permeability and shape of the NT.
  - Develop the experimental procedure for measurement of fast changes in mechanical parameters (bending rigidity and lateral tension) of the NT membrane using electro-actuation.
  - Quantify membrane deformations produces by Dyn1 and its mutants on short NTs.

- Using short, mechanically calibrated NTs, characterize membrane deformations by transition-state-mimic conformer of Dyn1 (developed in collaboration with Dr. Schmid lab) responsible for production acute membrane stresses leading to fission.

- Characterize regulation of Dyn1 activity by membrane curvature using "rigid" membrane templates: lipid bilayers supported on SiNW of calibrated diameters.

    - Develop experimental procedures for making supported lipid bilayer on surfaced-adhered SiNW.
    - Characterize interaction of Dyn1 with the SiNW-based lipid templates.

2. MATERIALS AND METHODS

2.1. Equipment and materials

2.1.1. GUV formation

- Vortex: $2x^3$, Velp Scientifica, Italy.
- Teflon® film: Teflon® film 0.02′′ thick, 24′′ wide, VS002X24, Fluoro-plastics Inc., USA.
- Beads:
  - Silicon Oxide Microspheres, 20 μm diameter, C-SI-O-20, # 140248, Corpuscular, USA.
  - Silicon Oxide Microspheres, 41 μm diameter, C-SI-O-40, # 140256 Corpuscular, USA.
- Rotary evaporator: vv micro, Heidolph, Germany.
- Peristaltic Pump: 2C 7.0mbar, Vacuumbrand, Germany.
- MT-30, Microtorch, Master appliance Corp., USA.
- Microcentrifuge tubes: Safe-Lock Tubes, 1,5mL, Eppendorf, Germany.
- Parafilm, 4′′ Parafilm ® M Barrier Film, SPI supplies, USA.
- 35mm petri dishes, S01775, Thermo Fisher Scientific, USA.
- Thermostatic Bath: S-22, Labolan, Spain.
- Cover glass No.1, 25mm diameter glass covers, Assistant, Germany.
- Sticky tape, Secure Seal Adhesive Sheet SA-S-1L, #620001, Grace

Bio-Labs, USA.

- Coverslip chamber 25mm, Science products, Germany.
- Argon compressed gas, Alphagaz, Air Liquide, France.
- Liquid nitrogen, Air Liquide, France.

2.1.2. LUV formation

- Vortex shaker: 2x^3, Velp Scientifica, Italy.
- Rotary evaporator: vv micro, Heidolph, Germany.
- Peristaltic Pump: 2C 7.0mbar, Vacuumbrand, Germany.
- Cone sonicator: Soniprep 150, MSE, Sanyo, Japan and Process Timer, MSE, Sanyo, Japan.
- Heating Magnetic Stirrer: ARE, Velp Scientifica, Italy.
- Mini-Extruder with heating block, #610000, Avanti Polar Lipids Inc., USA.
- Mini extruder filters 0.1 µm, PC MB 19MM .1UM, #800309, Whatman, UK.
- Mini extruder filters 0.4 µm, PC MB 19MM 0.4UM, #800282, Whatman, UK.
- Mini extruder filter supports, #610014, Avanti Polar Lipids Inc., USA.
- Microcentrifuge tubes: Safe-Lock Tubes, 1,5mL, Eppendorf, Germany.
- Parafilm, 4’’ Parafilm ® M Barrier Film, SPI supplies, USA.
- Argon compressed gas, Alphagaz, Air Liquide, France.

- Liquid nitrogen, Air Liquide, France.

2.1.3. SUV formation

- Vortex shaker: $2x^3$, Velp Scientifica, Italy.
- Rotary evaporator: vv micro, Heidolph, Germany.
- Peristaltic Pump: 2C 7.0mbar, Vacuumbrand, Germany.
- Cone sonicator: Soniprep 150, MSE, Sanyo, Japan and Process Timer, MSE, Sanyo, Japan.
- Microcentrifuge tubes: Safe-Lock Tubes, 1,5mL, Eppendorf, Germany.
- Parafilm, 4'' Parafilm ® M Barrier Film, SPI supplies, USA.
- Argon compressed gas, Alphagaz, Air Liquide, France.

2.1.4. BLM formation

- 300 mesh gilded grids for electron microscopy, G2076, New 300, 3.05mm, Athene Agar Scientific, UK.
- Painting brush: Martre Kolinsky Brush 3/0, 8404, Raphael, France.
- Microcentrifuge tubes: Safe-Lock Tubes, 1,5mL, Eppendorf, Germany.
- Thermostatic Bath: S-22, Labolan, Spain.
- Cover glass No.1, 25mm diameter glass covers, Assistant, Germany.

- 35mm petri dishes, S01775, Thermo Fisher Scientific, USA.
- Sticky tape, Secure Seal Adhesive Sheet SA-S-1L, #620001, Grace Bio-Labs, USA.
- Argon compressed gas, Alphagaz, Air Liquide, France.
- Nitrogen compressed gas, Air Liquide, France.
- Coverslip chamber 25mm, Bioscience Tools, USA.

2.1.5. Glass micropipettes fabrication

- Thin wall capillary with (TW150F-4, World Precision Instruments Inc., USA) and without filament (GB 150-10, Science Products, Germany).

- Micropipette pullers:

  - Model P-2000, Sutter Instrument Co., USA.
  - Model PB-7, Narishige, Japan.

- ID 03 inverted microscope (Zeiss instruments, Germany) with the following objective lenses:

  - F-LD 20/0.25, Zeiss instruments, Germany.
  - F-LD 32/0.4, Zeiss instruments, Germany.

- MicroFil™ syringe needle 28 gauge (MF 28G-5) and 34 gauge (MF 34G-5), World Precision Instruments Inc., USA.
- Syringes of several sizes, BD Plastipak, USA.

2.1.6. Micromanipulation

- Motion Controller; Model 860-C2, Newport, USA.
- Motor CMA-25CC, 991238, Newport, USA.
- Model PZC-SB, NanoPZ Series, Newport, USA.
- Model ESA-CSA, µ Drive Controller, Newport, USA.
- Motor PZA 12, Newport, USA.
- Bases, Clamps, Brackets, Support Rods and Optical mounts, Newport, USA.

2.1.7. Optical microscopy

- IX-70 inverted microscope, Olympus, Japan. Equipped with the following objectives lenses:
    - UPlanFL N 10X/0.30, Olympus, Japan.
    - LUCPlan FL N 40X/0.60, Olympus, Japan.
    - UAp o 150X/1.45 Oil TIRFM, Olympus, Japan.
- iXon EM+ Camera, Andor, Ireland.
- Fluorescence lamp, Series 120PC Q, X-Cite, Lumen dynamics, USA.
- PC workstations, Dell Inc., USA.
- Optical table, Newport, USA.
- Fluorescence filters:

  - 560/585, FF560/25 TRITC, Semrock, USA.
  - 485/505, FF01-485/20 FITC, Semrock, USA.
  - 649/662, FF01-649/13 CY-5, Semrock, USA.

2.1.8. Conductance measurements setup

- Oscilloscope: TDS 3014, Tektronix, USA.
- Patch Clamp Amplifier: Axopatch 200B, Axon Instruments, USA.
- PC workstations, Dell Inc., USA.
- ELECTRODES:
  - Ag/AgCl pellet electrodes:
  - ▪ Ag/AgCl pellet electrodes #EP02, World Precision Instruments Inc., USA.
  - ▪ Ground electrode: Disk 4mm dia. X 1mm, 10mm exposed wire, E-202, Science Products, Germany.
- Teflon coated silver wire for electrode preparation:
  - ▪ 75um uncoated dia. 140um coated dia. 7.5m, AG-3T, Science Products, Germany.
  - ▪ 250um 10ft, AGT1010, World Precision Instruments Inc., USA.
- MICROELECTRODE HOLDERS:
  - 45º Angle holder with port 1mm outer dia., HUW-P-1.0-45,

Science Products, Germany.

- 45º Angle holder with port 1.5mm outer dia., HUW-P-1.5-45, Science Products, Germany.
- Holder with port 1mm outer dia., HUW-P-1.0, Science Products, Germany.
- Holder with port 1.5mm outer dia., HUW-P-1.5, Science Products, Germany.
- Holder without port 1mm outer dia., HUW-0-1.0, Science Products, Germany.
- Holder without port 1.5mm outer dia., HUW-0-1.5, Science Products, Germany.

2.1.9. Other equipment

- Balances:
    - CP32025, Sartorius, Germany.
    - CP225D, Sartorius, Germany.
    - ME36S-0CE, Sartorius, Germany.
- pH paper, Macherey-Nagel, Germany.
- Osmometer: Cryoscopic osmometer, Osmomat 300, Gonotec, Germany.
- Bath sonicator: FB15049, Fisher Scientific, Thermo Fisher Scientific, USA.
- Shaker: Bio Shaker 3D, Biosan, Latvia.

- Centrifuges:
  - Sprout, Mini-Centrifuge, Heathrow Scientific, UK.
  - Minispin plus, Eppendorf, Germany.
- Ultrapure water purification system TKA Smart 2 Pure, TKA, Thermo Fisher Scientific, USA.
- Variable Volume Single Channel Pipettes, 0.1-2, 2-20, 20-200, 100-1000, Discovery Comfort, HTL, Germany.
- Plate Reader, Synergy HT, BioTek Instruments Inc., USA.

2.1.10. Proteins

Wild type Dynamin I and its mutants have been kindly provided by the group of Dr. Sandra L. Schmid from the UT Southwestern Medical Centre in Dallas, Texas, USA. The proteins were obtained via purification from peripheral membrane extracts of sheep brain using ammonium sulphate precipitation and affinity purification method on recombinant SH3 domains (Quan and Robinson, 2005), and checked for purity and GTPase activity. Mutations were performed by using commercially available kits.

2.1.11. Lipids

- 1,2-dioleoyl-sn-glycero-3-phosphocholine, DOPC, Ref# 850375, Avanti Polar Lipids Inc., USA.
- 1,2-dioleoyl-sn-glycero-3-phosphoethanolamine, DOPE, Ref# 850725, Avanti Polar Lipids Inc., USA.
- 1,2-dioleoyl-sn-glycero-3-phosphoethanolamine-N-(lissamine rhodamine B sulfonyl) (ammonium salt), Rh-DOPE, Ref# 810150, Avanti Polar Lipids Inc., USA.
- Cholesterol, Ref# 700000, Avanti Polar Lipids Inc., USA.
- 1,2-dioleoyl-sn-glycero-3-phospho-L-serine (sodium salt), DOPS, Ref# 840035, Avanti Polar Lipids Inc., USA.
- L-ɑ-phosphadidylinositol-4,5-bisphosphate (Brain, Porcine) (ammonium salt), PI(4,5)P, Ref# 840046, Avanti Polar Lipids Inc., USA.

2.1.12. Buffers and buffer components

- KCl, Potassium Chloride, SigmaUltra, Ref#P9333, Sigma-Aldrich, USA.
- HEPES Buffer 1M solution pH 7.3, Ref# BP299, Fisher Bio reagents, Thermo Fisher Scientific, USA.

- EDTA, Ethylenediaminetetracetic acid solution 0.5M, pH 8.0 Ref# 03690, Fluka, Sigma-Aldrich, USA.
- $MgCl_2$, Magnesium Chloride solution 1M, Ref# 63069, Fluka, Sigma-Aldrich, USA.
- Sucrose, Ref# 84097, Sigma, Sigma-Aldrich, USA.

2.1.13. Organic solvents

- Chloroform for HPLC, Ref# 366927, Sigma-Aldrich, USA.
- Methanol NORMAPUR, Ref# 20847, VWR, USA.
- Ethanol EMSURE, Ref#100983, Merk Millipore, USA.
- Decane, anhydrous, Ref# 457116, Sigma-Aldrich, USA.
- Octane, Ref#74822, Fluka, Sigma-Aldrich, USA.
- Squalane, Ref# 85629, Fluka, Sigma-Aldrich, USA.

2.1.14. Nucleotides

- Na GTP, Guanosine 5′-triphosphate sodium salt, Ref# G5884, Sigma, Sigma-Aldrich, USA.
- Li GTP, Guanosine 5′-triphosphate lithium salt, Ref# G5884, Sigma, Sigma-Aldrich, USA.
- Na GDP Guanosine 5′-diphosphate sodium salt, Ref# G7127, Sigma,

Sigma-Aldrich, USA.

- GMPPCP β,γ-Methyleneguanosine 5’-triphosphate sodium salt, Ref# M3509, Sigma, Sigma-Aldrich, USA.

2.1.15. Other materials

- BCA Protein Assay Kit: 23227, Thermo Fisher Scientific Inc., USA.
- Slide A Lyzer, Mini Dialysis Units 69570, Thermo Scientific, USA.
- Spin Desalting Columns: 89882, Thermo Fisher Scientific, USA.
- Amber Vials Screw Top 4 mL PTFE Liner, 27001-U, Supelco, USA.

2.1.16. Data acquisition software

- Electrical admittance acquisition: Bronew 32, version 5.0, (Ratinov et al., 1998).

- Microscope camera software: Micro-Manager 1.3, version 4, Micro-Manager, NIH, USA (Fryer, 2004).

2.1.17. Analytical software

- Image J 64, 1.46e, NIH, USA (Schneider et al., 2012).
- Origin 7 SR2, OriginLab Inc., USA.

2.2. Methods

2.2.1. Preparation of multilamellar vesicles

The starting point for the preparation of all types of the vesicles used in this work was production of the multilamellar vesicles (MLV). The basic composition for the MLV was DOPC:DOPE:DOPS:Chol:PI(4,5)P 28:25:15:30:2 mol%. In the experiments with electric field-driven expansion of the NTs pulled from GUV no-charge lipid composition (DOPC:DOPE:Chol 60:10:30 mol%.) was used to avoid electro-osmotic effects. For the GUV preparations 0.1-0.5 mol% of fluorescently labeled lipid Rh DOPE was added to the basic composition. The amount of total lipid used varied dependently of the type of vesicles used as described in Table 2.1.

Type of liposome	Total lipid (mg)	Final volume (μL)
SUV for LUVs (0,5g/L)	0,125 mg	250 μL
GUV (0.5g/L)	0,05 mg	100 μL

Table 2.1. Lipid concentration by type of liposome preparation.

MLVs were usually prepared in a 1 mL round bottom flask suitable for the rotary evaporator. Lipids stocks in chloroform (except for PI(4,5)P, which is diluted in a special mixture of chloroform:methanol:water 20:9:1 (vol/vol) were mixed to the desired concentration and quantity. The mixture was dried under vacuum for 1h and then the lipids were resuspended in chloroform:methanol, 9:1 (vol/vol). This mixture was used to produce a thin lipid film using rotary evaporator (1 h under vacuum) with a round-bottom flask. MilliQ grade water (SUV and GUV preparation) or ionic buffer (LUV preparation) was then added to the flask in the quantities indicated in Table 2.1. After 15 to 30 minutes hydration of the lipid film at 60ºC the flask was gently shacked (using vortex) to detach the lipid film from the glass thus resulting in MLV formation.

2.2.2. Formation of GUVs

We used a modified version of the gentle-hydration protocol (Reeves and Dowben, 1969) to produce GUVs attached to the surface of 40 μm silica beads. 10 μL of MLV were separated into 4 small drops on a pre-cleaned Teflon film surface. 3 μL of the silica bead suspension (10% vol/vol) were added to each drop by gently touching the drop surface by the pipette tip containing the beads. Then the drops were dried under vacuum for 15 minutes (Figure 2.1.).

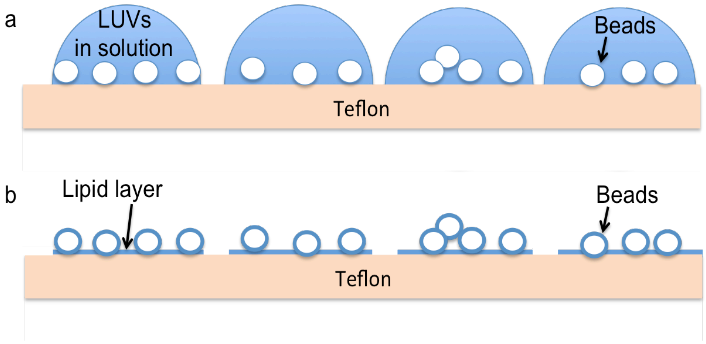

Figure 2.1. Lipid layer formation over silicon beads. a) 4 drops of LUV solution are deposited over a pre-cleansed Teflon surface. The beads are introduced inside the drops by gently touching the surface of the drop with pipette tip containing the beads. b) The lipid layer is formed over the beads upon vacuum drying of the drops from a.

Then, the lipid films covering the beads were subjected to gentle hydration following the protocol depicted in Figure 2.2. We used a fire-closed glass micropipette to scrape a small amount of beads from the Teflon film and to deposit them into a vertically held 20 µL plastic tip. This tip was previously cut at its 2 µL level and was pre-filled with 5 µL of 1 M sucrose solution. Once the micropipette touched the surface of the sucrose solution in the tip, the beads started floating towards the bottom of the tip and the lipid films on the beads started swelling. To ensure the maximal swelling of the films required for the GUV production the tip was placed for 5′ to a thermostat kept at 60 – 70 ºC. GUVs remained attached to the beads or detached as free-floating vesicles dependently on the time and temperature of the incubation. For electrical recordings combined with fluorescence microscopy we used shorter incubation times so that most of the GUVs remained attached to the beads. The beads with GUVs were then transferred to the microscopy observation chamber filled with the working buffer (150 mM KCL, 10 mM HEPES, 1 mM EDTA, 2 mM $MgCl_2$). The surface of the buffer was gently touched with the pre-cut tip containing the swollen GUVs (Figure 2.2.). The beads and GUVs quickly reached to the bottom of the observation chamber driven by gravity.

The observation window of the chamber was made of a thin coverslip glass (diameter 25 mm, 0.17 mm thick) pre-treated with bovine serum albumin (BSA) to minimize lipid adhesion to the coverslip. The pre-treatment was done by covering the coverslips with 0.2 g/L solution of BSA for 5′ followed by 3-time washing with MilliQ grade water. The observation chamber was mounted on the stage of the Olympus IX-70 inverted microscope (last cartoon of the Figure 2.2.). The GUVs labeled with Rh-DOPE were approximately of the same size as the beads, 20-40 µm in diameter.

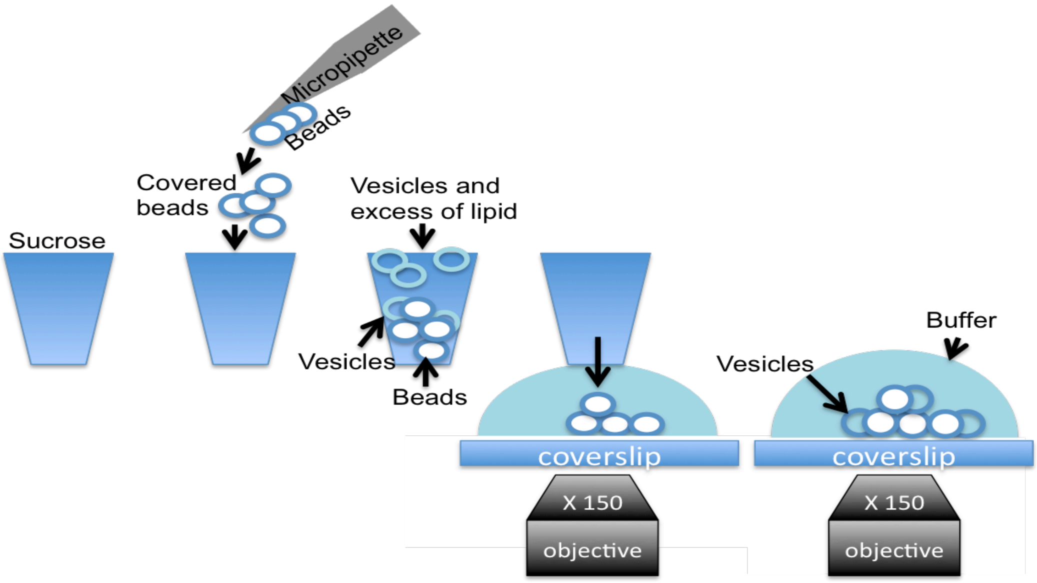
Micropipette
Beads
Covered beads
Sucrose
Vesicles and excess of lipid
Vesicles
Beads
Buffer
Vesicles
coverslip
X 150
objective
coverslip
X 150
objective

Figure 2.2. Main steps in supported GUV formation protocol. Beads covered by the lipid film are gently introduced by a micropipette into a vertically held pipette tip prefilled with 1 M sucrose. The gravity makes the beads go to the bottom of the tip. Hydration of the lipid film on the beads is spontaneous and GUVs start growing immediately. Finally, by gently touching the surface of the buffer, the beads with supported GUVs are transferred to the observation chamber and are deposited on a thin coverslip, thus allowing for their direct observation with a high magnification objective using an inverted microscope.

2.2.3. Preparation of Small Unilamellar Vesicles

SUVs were prepared by tip sonication of MLVs for 10 cycles of 15’’ on, 45’’off with the amplitude of 4 μA. The sonication produced SUVs of diameters between 20 and 50 nm.

2.2.4. Formation of LUVs

We prepared LUVs from SUVs by a freeze-thaw procedure (6 cycles of freezing in liquid N_2 followed by thawing in RT water) followed by extrusion through a polycarbonate filter with calibrated pores (diameter 100 or 400 nm). The protocol is depicted in Figure 2.3.

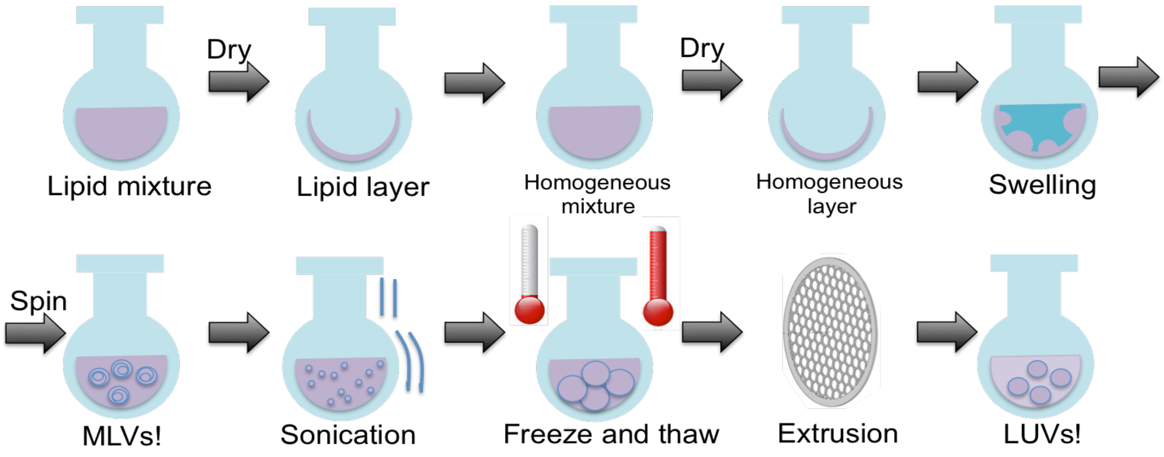
Dry
Dry
Lipid mixture
Lipid layer
Homogeneous mixture
Homogeneous layer
Swelling
Spin
MLVs!
Sonication
Freeze and thaw
Extrusion
LUVs!

Figure 2.3. Main steps in LUV preparation. The lipids are mixed in their original solvents (chloroform, except for PI(4,5)P, which contains also methanol and water), which are evaporated under vacuum. The resulting lipid film is re-dissolved in a chloroform:methanol solvent mixture in order to obtain good wettability and better homogeneity of the mixture. The lipid film resulting from the second solvent evaporation in a rotary evaporator is hydrated with the working buffer. The swelling of the film yields MLVs. The MLVs are subjected to sonication in order to obtain SUVs. The SUVs are exposed to 6 cycles of freeze and thaw, what allows for their fusion together, forming bigger size unilamellar vesicles. The final step in LUV formation consists in vesicle size adjustment by extrusion through a filter with a desired pore size.

2.2.5. Preparation of planar bilayer lipid membranes (BLMs)

For production of so called black lipid membranes (BLM) we used a modified Mueller and Rudin procedure (Mueller, 1967). The method consists of “painting” the mixture of lipids in an organic solvent over a hole in a Teflon partition using a small brush (Frolov et al., 2003; Melikyan G. B., 1982). The lipid compositions used are listed in Table 2.2.

Composition	**Mol ratio**
DOPC: DOPE: Chol	40:30:30
DOPC: DOPE: DOPS:Chol: PI(4,5)P	28:25:15:30:2

Table 2.2. Mol ratio data of the BLMs used in this work

We used electron microscopy gilded grids (300 mesh, 54 x 54 um holes, Figure 2.4) as the partition for the BLM. The grids were pre-treated with 2 µL of the lipid mixture in decane:octane (“pre-painting” mixture, see below) and dried under a N_2 flux. Pre-treated grids were mounted onto the coverslip of the observation chamber using two small rectangular sticky tapes (1,5 mm x 4 mm approximately). The chamber was then mounted on a stage of an inverted microscope (Olympus IX-70) and slowly filled with the working buffer (150 mM KCL, 10 mM HEPES, 1 mM EDTA, 2 mM $MgCl_2$) to avoid air bubbles trapped between the grid and the sticky tapes. BLMs were formed upon smearing a small drop of the "painting" lipid mixture over the pre-treated grid with a small brush (triple zero sable kolinsky is recommended). We used a 10X or 20X microscope objective and the phase contrast to monitor the BLM formation. After few seconds the spontaneous formation of BLMs in many of the grid holes was observed.

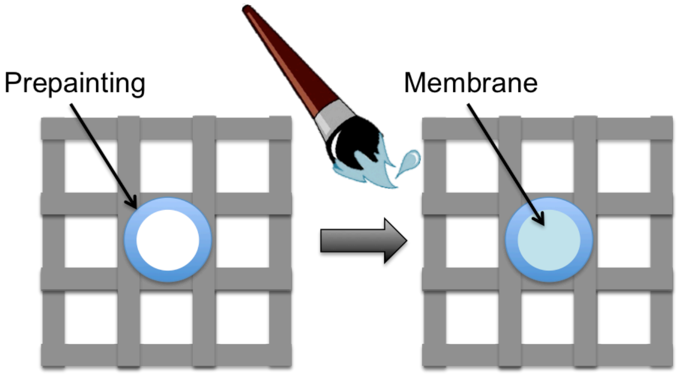

Figure 2.4. Schematic representation of black lipid membrane formation. A brush is used to "paint" a BLM over the pre-treated hole of a gilded grid.

The "pre-painting" and "painting" lipid mixtures were prepared daily and kept at +4C^0. The lipids (table 2.2.) were dissolved in decane:octane 1:1 (pre-painting) or squalane (painting) at the concentration of 20 mg/mL. The lipid stock solutions were first mixed in two eppendorf microcentrifuge tubes and the original solvent was evaporated under an argon flux. Then, 20 µL of octane and 20 µL of decane were added to one eppendorf tube to make the “pre-painting” mixture. 40 μL of squalane was added to another eppendorf to make the “painting” mixture. The eppendorf tubes were subjected to vigorous vortexing to dissolve the lipids. To ensure the transfer of lipids into squalane we generally started from squalane:octane mixture 1:1 (vol/vol); upon obtaining homogeneous mixture, we removed the octane, which is much more volatile than squalane, using N_2 or argon flux.

2.2.6. Measurements of electric conductance of NTs formed from BLMs

To pull the NTs we used patch-clamp borosilicate glass pipette produced as described elsewhere (Lollike and Lindau, 1999). The electrical resistance of the pipettes was around 1 MOhm, corresponding to the tip diameter of ~1 μm. Depending on the assay, the pipettes contained the working buffer or the protein diluted in the working buffer. We approached the BLM using calibrated nanomanipulator. The approach was monitored by bright-field microscopy using 20X objective lens (Figure 2.5.). The electrical potential of the electrolyte in the observation chamber was kept at 0 using Ag/AgCl pellet ground electrode connected to a patch-clamp amplifier. The measuring electrode was put inside the pipette so that the pipette resistance was controlled during the approach using voltage-clamp mode of the amplifier. Once the pipette touched the membrane, its resistance quickly increased to 10-100 GOhm, indicating formation of tight contact between the membrane and the rim of the pipette tip (so called gigaseal contact, Neher and Sackmann, 1992).

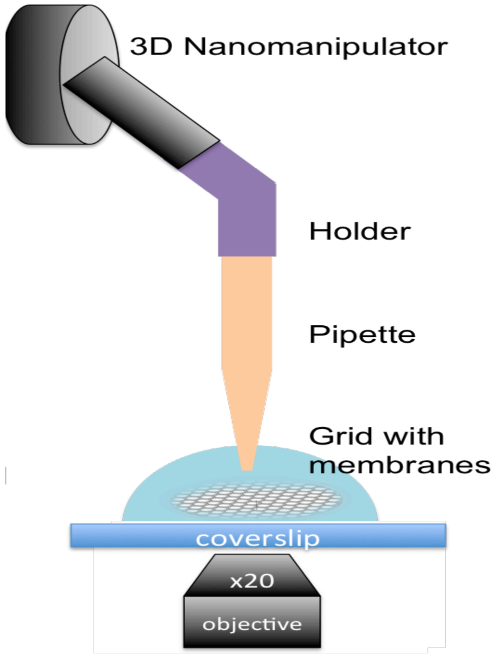

Figure 2.5. Patching configuration for BLMs. In order to pull a NT, the patching pipette is set to be normal to the BLM. The pipette is attached to a 3Dnanomanipulator, thus allowing for fine control of its movements. BLM approach is monitored with a 20x objective of the stage of an inverted microscope.

Then we applied negative pressure through the lateral port of the holder for breaking the membrane patch isolated inside the pipette. Generally, the patch rupture did not affect the stability of the BLM. Hence, by slowly moving the pipette away from the membrane we pulled a membrane tube (step 4 in Figure 2.6.b). With the pipette moving away from the membrane, the initial catenoid tube collapsed and the cylindrical NT formed (see Introduction section). The NT formation was seen as characteristic abrupt conductance decrease (Figure 2.6.b). The NT conductance was further monitored using voltage-clamp mode of the patch-clamp amplifier with 50-100 mV holding potential and 100 mV/pA amplification. Note that the high lateral tension of the BLMs suppressed the membrane fluctuations typical for more relaxed membrane systems (such as GUVs), thus allowing for formation of stable NT of submicron length.

Upon the NT formation the NT could be monitored through the measurement of ionic current (I_{meas} in Figure 2.6. a) passing through the inner lumen of the NT. The equivalent circuit for this system is detailed in the Figure 2.6.a. The electrode was placed in the inner part of the glass pipette. The pipette lumen constitutes the first resistance of the circuit (dashed rectangle in red in Fig. 2.6.a); because of the large size of the pipette (compared to the NT) this resistance is negligible in the most of the experiments. The resistance of the lipid-glass contact R_{leak} determines the amount of the leakage current going away from the NT, the current value depends on the “patch quality” or the tightness of glass-membrane contact. Finally, the NT lumen constitutes R_{NT} (both resistances are detailed in Figure 2.6.a). The ground electrode that is immersed in the working buffer closes the circuit. R_{leak} can be determined at the stage of the patch formation only

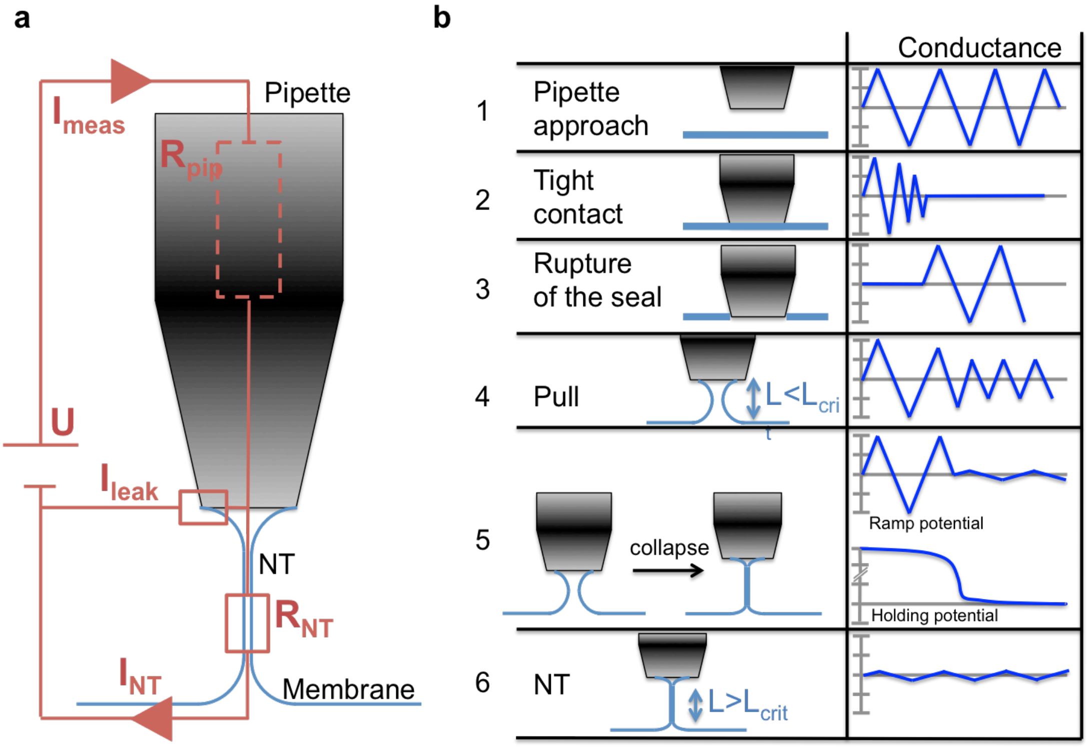
a
I_{meas}
Pipette
R_{pip}
U
I_{leak}
NT
R_{NT}
I_{NT}
Membrane
b
Conductance
1
Pipette approach
2
Tight contact
3
Rupture of the seal
4
Pull
L<Lcri
5
collapse
Ramp potential
Holding potential
6
NT
L>Lcrit

Figure 2.6. Electric conductance during and after NT formation. a) Equivalent circuit used for electric conductance measurements of a NT. The membrane is represented in blue and the ~1 μm in diameter pulling pipette containing a measuring electrode is represented in grey. A ground electrode immersed in the solution closes the circuit (not shown). R_{pip} and R_{NT} are the electric resistances of the pipette opening and of the NT respectively. I_{leak} and I_{NT} is the electric current going through the membrane-pipette contact site (leakage) and the NT, respectively. U is the applied potential and I_{meas} is the measured current corresponding to the sum of I_{NT} and I_{leak}. b) I_{meas} behavior during formation of the NT from a BLM. 1) During the pipette approaching stage we apply ramp holding potential. 2) Upon the gigaseal is formed the I_{meas} drops to its background level. 3) The breakage of the seal by negative pressure restores the current to its pre-seal level. 4) When the pipette starts to move out of the BLM, the catenoid forms and the I_{meas} becomes smaller. 5,6) Finally, the catenoid collapses and the NT forms, thus the I_{meas} abruptly drops reaching the $I_{NT}+I_{leak}$ level (equivalent circuit from a).

the membranes with sufficiently large and stable R_{leak} were used in the assays. The measured current is determined by:

$$I_{meas}(L) = I_{leak} + \frac{U}{R_{NT}(L)} \qquad \text{(Eq. 2.1)}$$

The equation 2.1. indicates that I_{meas} depends on the length of the NT. Indeed the correspondence between NT length changes and changes in I_{meas} was routinely used as a checkpoint to confirm the existence of a NT (Figure 2.7.).

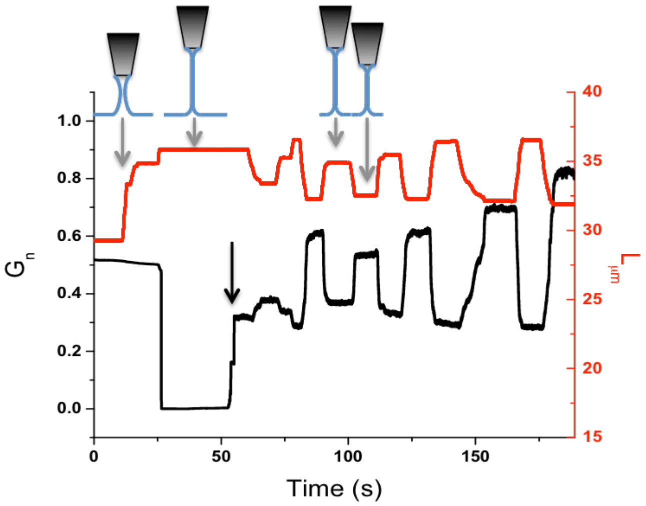

Figure 2.7. Conductance and length correspondence in a membrane NT indicate the existence of a NT. Pipette displacement is indicated in red, while the measured conductance normalized to the initial NT conductance is indicated in black. First the pipette was moved away from the membrane (first length increase) until the conductance dropped to its (I_{NT}+I_{leak}) level (as described in Fig. 2.6. above). This drop corresponded to the "collapse" of the catenoid and formation of a NT (step 5 in Fig. 2.6.b). At the point indicated by the black arrow, the applied holding potential was increased in order to have more measurement sensitivity. Following, several cycles of NT length decrease/increase were performed and the correspondence between length/conductance changes was monitored.

We also routinely checked the long-term stability of the NT conductance (Figure 2.8.).

Figure 2.8. Stability of I_{meas} in time. An example of NT stability control is shown.

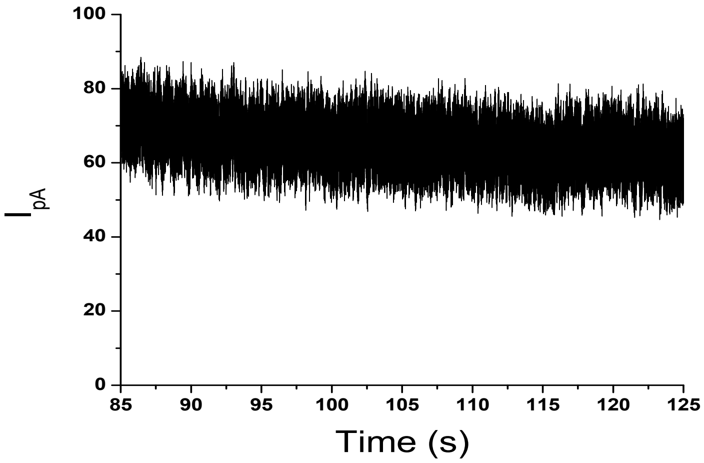

2.2.7. Preparation of supported bilayers on SiNWs

Silicon nanowires were used to create locally cylindrical membrane templates with fixed curvature. Formation of supported bilayers on silicon nanowires is well understood (Artyukhin et al., 2005; Geng et al., 2014; Huang et al., 2007; Misra et al., 2009; Noy, 2011; Tunuguntla et al., 2014). The diameter of the wires can be controlled with ~5nm precision, thus allowing us to control the geometric curvature of the supported lipid layers.

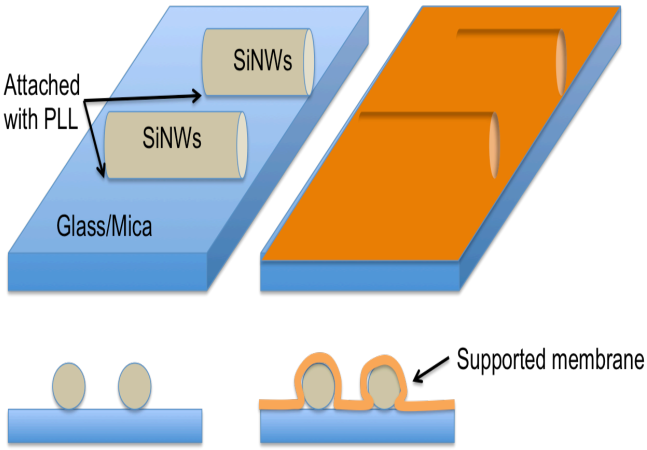

Figure 2.9. Formation of supported bilayers over SiNW. First, the SiNW are deposited on glass or mica surface pre-coated with Poly-L-Lysine (PLL). Addition of SUVs to the adhered SiNW results in formation of continuous supported bilayer over the template.

To produce the SiNW-supported lipid bilayers we used the following protocol. Freshly cleaved mica or a 0.17mm glass coverslip (pre-cleansed by sonication in EtOH followed by 30′ boiling in MilliQ grade water) were treated with 0.1% poly-L-lysine (PLL) solution for 15′ to achieve a coating. 3-time washing in MilliQ water and drying in vacuum followed the incubation with PLL. Simultaneously, SiNWs were detached from the mother wafer by gentle bath sonication in EtOH for 1´. 10 μL of SiNW in EtOH were added to the glass or mica substrate and the EtOH was quickly evaporated in vacuum. Subsequently, 20 μL of LUV solution (prepared on MilliQ water) was added to the attached SiNW and the sample was subjected to a 10′ incubation at RT to ensure the LUV binding to the wires. 1M $NaCl_2$ was added to the LUV solution to achieve a final concentration of 600 mM of $NaCl_2$. The electrolyte solution promoted the supported bilayer formation after 20´ of incubation. The sample was cleansed 3 times with MilliQ water and left with working buffer.

2.2.8. Fluorescence microscopy imaging of GUV-NT and SiNW templates

We used Olympus IX-70 inverted fluorescence microscope equipped with Andor iXon EM+ Camera, controlled by MicroManager software. 150X/1.45NA objective lens was used to maximize photon collection efficiency. The Series 120PC Q, X-Cite, excitation lamp was used at low power to minimize bleaching. 560/585 filter (FF560/25 TRITC) was used to monitor the lipid marker (Rh-DOPE), while 485/505 (FF01-485/20 FITC) or 649/662 (FF01-649/13 CY-5) were used to monitor dynamin conjugated with Alexa-488 or Alexa-647. The image sequences were collected at 10fps and analyzed off-line using ImageJ software.

2.2.9. Protein dialysis

Before each experiment, freshly unfrozen Dyn1 aliquots were dialyzed against the working buffer in order to avoid membrane instabilities during the experiment. The micro dialysis was performed by using the slide-A-Lyser MINI Dialysis devices (Pierce, USA) according to manufacturer instructions.

2.2.10. Measurements of the protein concentration

Upon protein dialysis, the commercially available Pierce kit for BCA assay was used for the colorimetric quantification of total protein present in the resulting Dyn1 sample. The formulation uses the combination of the biuret reaction (the Cu^{+2} to Cu^{+1} reduction by protein in an alkaline medium) and the colorimetric detection of the Cu^{+1} by the bicinchoninic acid (BCA). The used protein standard was the bovine serum albumin (BSA). The standard curve and the diluted protein unknowns were measured at 562 nm emission wavelength by using a plate reader.

2.2.11. Cross-linking of the protein

For chemically crosslink the cysteines of the CC mutant we used MTS-4-MTS crosslinker. The crosslinking reaction requires the removal of dithiothreitol (DTT) from the sample. This step was performed using commercially available desalting columns and following the protocol from fabricant (Pierce, USA). Briefly, we inverted the column to mix the slurry. Then we twisted off the bottom of the column, we placed it in an eppendorf tube and loosed the lid. The tube was then centrifuged at 1500rpm for 1 minute and the obtained liquid was discarded. Then 300 µL of buffer (150 mM KCL, 10 mM HEPES, 1 mM EDTA, 2 mM $MgCl_2$) was added to the column and it was centrifuged again discarding the obtained liquid. This last step was repeated three times. Then we added the protein (volume addition between 30 µL and 90 µL) and centrifuged it for two minutes. The obtained product was the DTT free protein sample.

The DTT free CC-Dyn1 sample was then crosslinked as following. Freshly unfrozen MTS-4-MTS reagent at 0.5 mM concentration was mixed 1:10 with the DTT free CC-Dyn1 sample and incubated 10 at room temperature. The obtained crosslinked protein was stable for more than two hours.

2.2.12. Measurements of the NT constriction and fission by Dyn1

The curvature creation by Dyn1 (membrane constriction or NT constriction) was monitored as decrease of either electrical conductance (Figure 2.10. a) or membrane fluorescence (Figure 2.11) of the NT (Shnyrova et al., 2013). The length of the NT was kept fixed and the conductance changes were monitored at a voltage-clamp mode applying 100mV holding potential. The fluorescence of the NT membrane was monitored as described using low-level excitation power to avoid photo damaging. The constriction is seen as appearance of dark regions (strata) in the tube. The fluorescence decreases as the membrane is squeezed away from the regions covered by Dyn1 helices (Shnyrova et al., 2013). The dark regions grow in the axial direction with progressive lengthening of the dynamin helices.

To monitor membrane fission Dyn1 was applied simultaneously with 1 mM GTP, the GTP was also added to the experimental chamber. An acute drop in conductance followed the NT constriction to the background level, corresponding to the closure of the NT (Figure 2.10).

The nanotube lumen closure and the complete fission cannot be distinguished from each other just with conductance measurements. For distinguishing them additional experimental information is required. We used fluorescence microscopy to confirm the complete disconnection of the NT. The assembly of the Dyn1, seen as expelling of membrane fluorescence of the NT, was always followed by a fast NT breakage. This correspondence between electrical and optical measurements confirms that the acute drop of the NT conductance to the background level (Figure 2.10) indicates the NT fission.

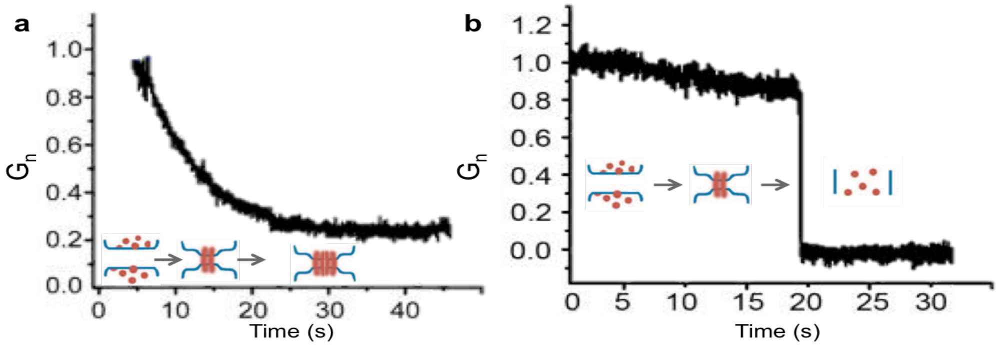

Figure 2.10. Conductance trace of a NT in the presence of wild type dynamin with and without GTP. a) Normalized conductance trace of an NT in the presence of Dyn1 is shown. Decrease in conductance indicates decrease of the NT radius. b) Conductance trace of an NT in the presence of Dyn1 and 1 mM GTP. Here the decrease in conductance is followed by an abrupt drop to its zero level, corresponding to the NT fission (Bashkirov et al., 2008).

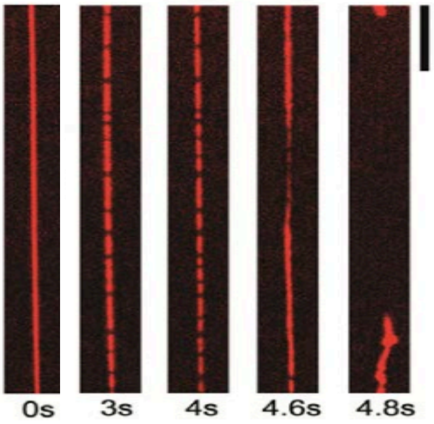

Figure 2.11. Time sequence showing the membrane fluorescence of a NT in the presence of wild type dynamin and GTP. RhDOPE fluorescence is shown. Adsorption of Dyn1 on the NT leads to the squeezing of the NT and the consequent expelling of the RhDOPE from the sites of constriction. Finally, the NT undergoes fission. Scale bar 10 μm. (From Shnyrova et al, 2013)

3. RESULTS AND DISCUSSION

3.1. Simultaneous measurements of ionic permeability and fluorescence of NTs pulled from GUVs

In this work we attempted for the first time to perform simultaneous measurements of fluorescence and ionic permeability of NTs pulled from a GUV. These measurements had two purposes: 1) elaborate a procedure for real-time measurements of membrane elasticity using electro-actuation; 2) quantify membrane constriction by proteins. We used fluorescently labelled GUVs supported on silica beads (sGUVs) (Figure 3.1.). To pull the NT from

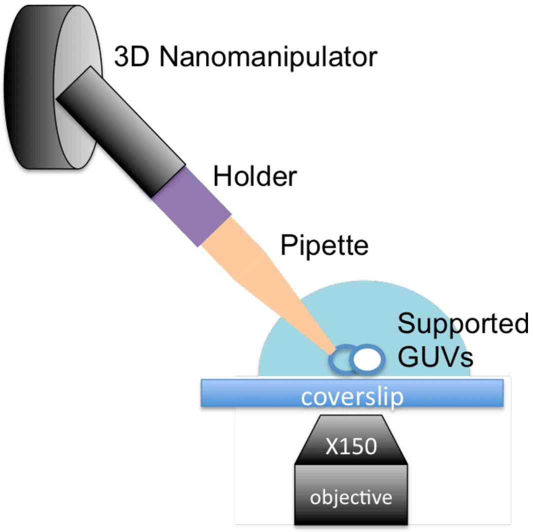

Figure 3.1. Patching configuration for GUVs. The patch pipette is held at a 45-degree angle respect to the coverslip. The proximity of the sGUV to the coverslip allows for the use of high mag objectives on an inverted fluorescence microscope.

sGUV we used a patch-clamp setup similar to the one described in the Methods section Figure 2.5. However, in the GUV system we used a 45º pipette holder in order to approach the GUVs from the side and further pull the NTs in horizontal direction. The proximity of the supported GUV to the coverslip of the observation chamber allowed fluorescence imaging of the NT employing optical lenses with high numerical aperture (NA) and magnification, e.g. 150x, 1.4NA (Figure 3.1.).

In the initial experiments with sGUVs we used simple non-charged lipid composition (DOPC:DOPE:Chol, see Methods). Patching of non-charged sGUVs revealed that, unlike free-standing GUVs, their interior is electrically connected to the external media (Figure 3.2.b). These electrical connections apparently emerge in the contact area between sGUV with the silica bead.

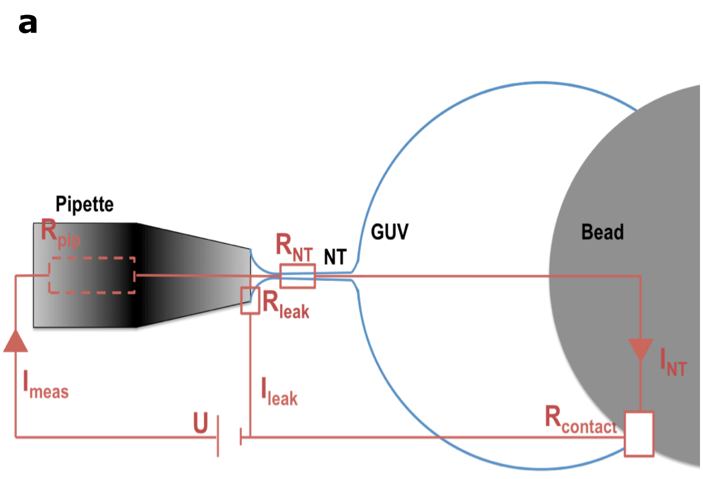

Figure 3.2. Equivalent circuit of a NT pulled from a GUV. a) The equivalent circuit is similar to the described in Figure 2.6.a, but an additional access resistance ($R_{contact}$) appears in the site of sGUV contact to the bead. In most cases, this resistance is small and allows for R_{NT} measurements. b) Changes in conductance during NT formation. On the left the corresponding images of

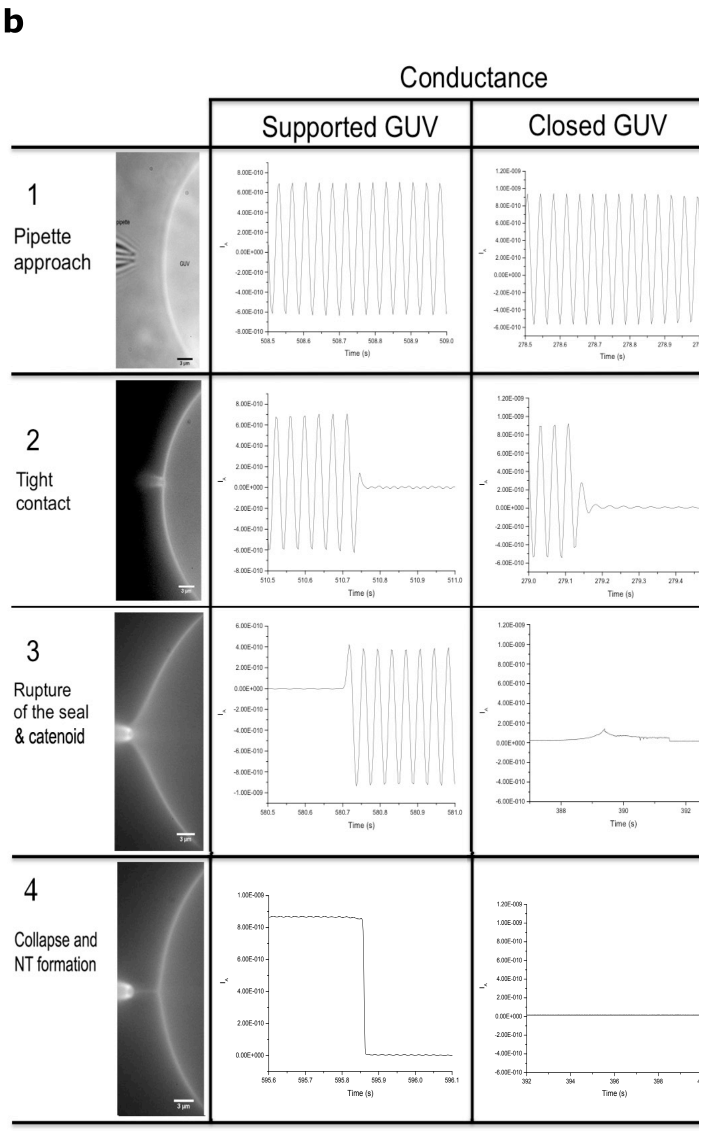

the pipette and sGUV surface are shown for each step. 1) Prior to the patch, the conductance characterizes R_{pip}. 2) Abrupt decrease of conductance to background level indicates the moment of the patch formation. 3) The following increase of conductance indicates the patch rupture by a pulse of negative pressure applied to the pipette interior. Note the absence of electrical connectivity in the case of GUVs. The conductance value after the patch rupture measure R_{pip} and $R_{contact}$ connected sequentially in the sGUV (see equivalent circuit in a). I_{after}/I_{before} ranged from 0.3 to approximately 1, demonstrating that $R_{contact}$ is smaller or comparable to R_{pip}. For NT measurements we used sGUVs with I_{after}/I_{before} close to 1. 4) Collapse and NT formation lead to an abrupt decrease in conductance for sGUVs.

Although we do not know the exact nature of this contact, we found that in the most of the experiments the integral electrical resistance $R_{contact}$ was comparable or smaller than the patch-pipette resistance as the changes in I_{meas} upon gaining the electrical access to the GUV interior ($\Delta I_{meas} \sim (U/R_{pip})*(R_{contact}/R_{pip})$) were generally small (see Figure 3.2.b). Hence, the equivalent electrical circuit of the sGUV system was similar to that of the BLM system. Similarly to the BLM system, I_{meas} depended on the length of the NT (Figure 3.3.). We found that application of 10-30 mV holding potential (with 1-10 mV/pA amplification) was sufficient to robustly measure the current changes corresponding to 1-10 micron changes in the NT length (Figure 3.3.).

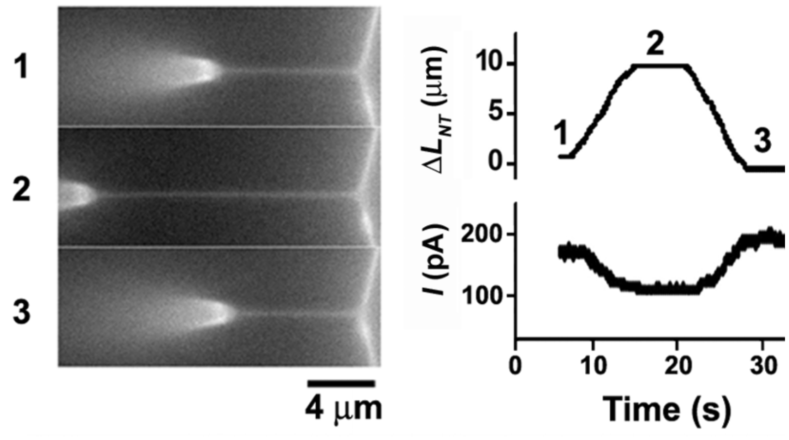

Figure 3.3. Variation of the NT conductance upon changes in NT length. Left panel shows fluorescence imaging sequence of a NT length changes. On the right the changes in length and in current are plotted for the same NT.

From the equivalent circuit (Figure 3.2.a), we deduced that

$$I_{meas}(L) = I_{leak} + \frac{U}{R_{NT}(L)} \qquad \text{(Eq. 3.1.)}$$

According to the Ohm´s law, the electrical resistance of the lumen of a cylindrical NT is:

$$R_{NT} = \frac{\rho \, L_{NT}}{A} \qquad \text{(Eq. 3.2.)}$$

where A is the cross-section area of the NT lumen and ρ is the working buffer resistivity ($\rho_{150mM\ KCl} = 66{,}6\ \Omega\ \mathrm{cm}$). We can rewrite Eq. 3.1 as:

$$I_{meas}(L) = I_{leak} + \frac{U\,\pi\, r_{NT}^2}{\rho\, L_{NT}} \qquad \text{(Eq. 3.3)}$$

where L_{NT} is set by the piezo-manipulator displacement. It follows that r_{NT}^2 can be obtained from the hyperbolic fit of $I_{meas}(L_{NT})$ as shown in Figure 3.4.a. The radii obtained from different GUVs ranged from 150 to 220nm.

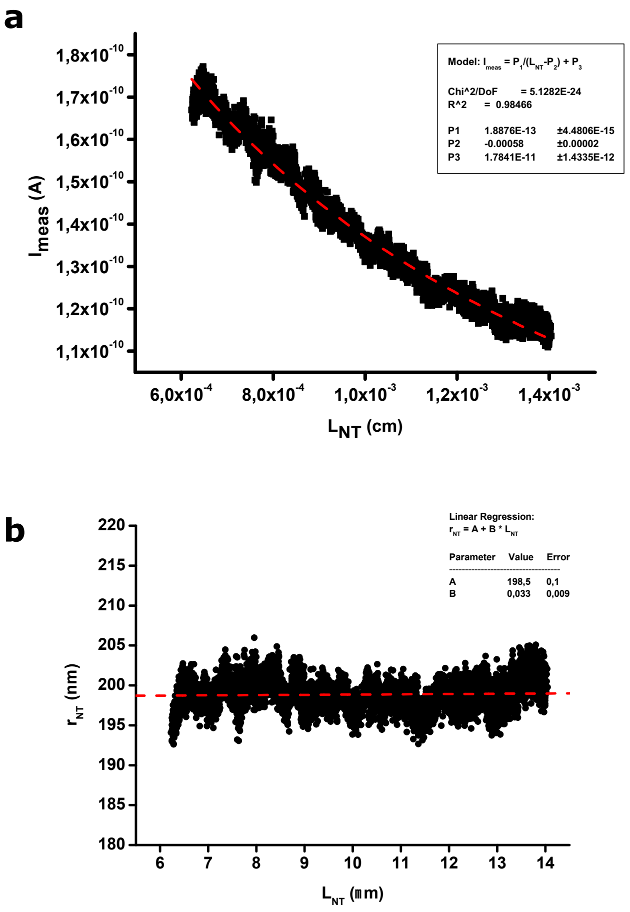

Figure 3.4. NT radius calculation. a) Hiperbolic fit of $I_{meas}(L_{NT})$ that allows to obtain the R_{NT} at a given U, as:

$$I_{meas} = \frac{U}{R_{NT}}$$

$$= \frac{U\,(\pi {r_{NT}}^2)}{\rho(L_{NT} - L_0)} + I_{leak}$$

$$= \frac{P_1}{L_{NT} - P_2} + P_3$$

where P_1, P_2 and P_3 are parameters resulting from the fit. b) With the parameters P2 and P3 determined by the fit in (a), we can plot $r_{NT}(L_{NT})$ as:

$$r_{NT} = \sqrt{\frac{\rho\, U}{\pi}(I_{meas} - P_3)(L_{NT} - P_2)}$$

The linearity of the plot confirms that the radius of the NT does not depend on its length. Red dashed lines indicate the fitting results.

Similar fitting procedure was earlier applied to the BLM system (Bashkirov, 2006). For BLMs made of the same lipid composition, the radii varied from 6 to 10nm, being approximately 10 times smaller than those in the GUV system. The difference in the NT radii corresponds well to the 100 times difference in lateral tension between the systems (Roux, 2013).

It has been suggested earlier that the electric field can affect the NT shape via electro-actuation, the process that can be defined as the movement of a membrane driven by trans-membrane electric field (Mosbacher et al., 1998). Using the NTs pulled from sGUVs we can directly verify this assumption and further quantify the shape changes. We note that according to the equivalent electrical circuit (Figures 3.2.a, 3.5), the trans- membrane field is different along the NT length. The applied potential has its maximum (equal to the applied holding potential U) near the tip of the patch pipette and it decreases till zero in the point of contact with the parent membrane (Figure 3.5.).

Figure 3.5. Deviation of a NT from cylindrical shape due to electro-actuation. A voltage is applied in the pipette electrode; this makes the electric field that passes through the NT (E1) and across the NT membrane (E2). The potential is zero in the connection point of the NT and the membrane and the red horizontal arrows indicate the decrease of the potential.

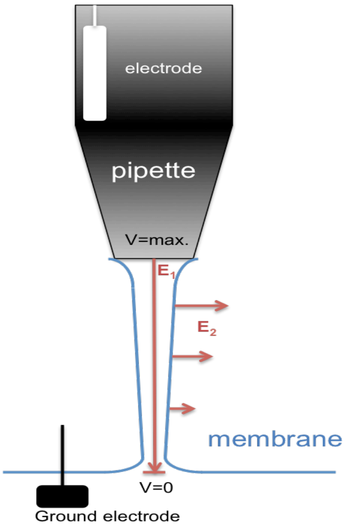

Figure 3.5 outlines the expected shape changes: the NT would expand non-evenly from the patch pipette toward the parent membrane. The level of the tube widening is expected to be proportional to the strength of the field (red arrows, Figure 3.5).

The NT expansion driven by electric field was evident form the analysis of the fluorescence microscopy images of the NTs pulled from GUVs (Figure 3.6.). In agreement with the field-driven expansion the fluorescence intensity integrated over a region of interest (ROI) including the whole NT gradually increased with the application of progressively bigger holding potentials (Figure 3.6.a). The NT expansion was noticeably large near the pipette tip so that the NT contours acquired the parabolic shape (Figure 3.6.b).

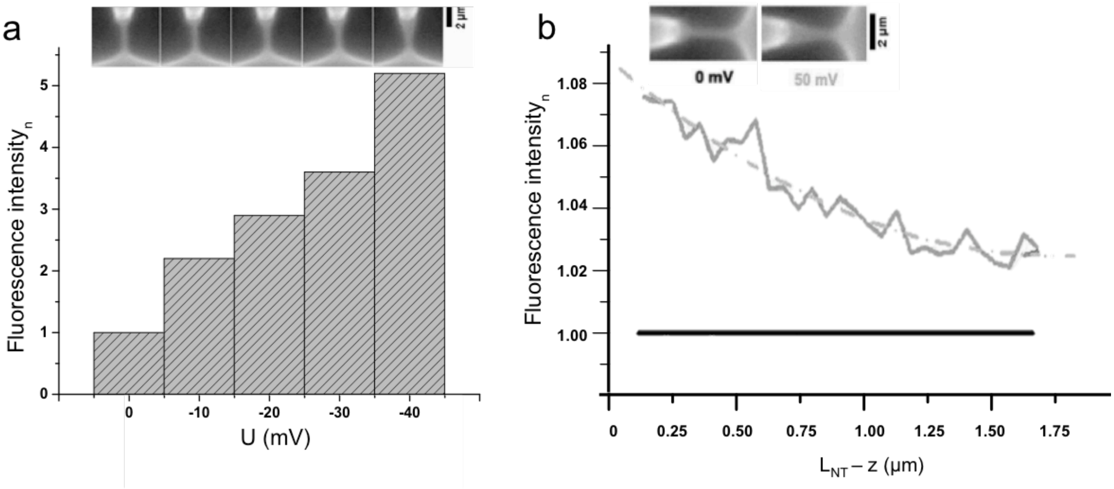

Figure 3.6. NT shape depends on applied voltage a) The widening of the NT upon different potentials was observed with fluorescence microscopy. Upper insert shows the fluorescence of RhDOPE within the membrane. More brilliant upper part corresponds to the pulling pipette. The fluorescence of the same ROI at different potentials, was normalized for the fluorescence of the NT at 0 mV. b) Analysis of the fluorescence of the NT along the NT axis upon 0 mV (black) and 50 mV (grey) potentials shows the change of NT shape upon bigger voltages. The grey dot and dash line indicates a parabolic fit.

To analyse the NT expansion quantitatively, we need to understand the driving forces behind the expansion. Earlier analysis (Bashkirov et al., 2008; Shnyrova et al., 2013) suggested that electro-capillary-like forces drive the NT expansion. The essence of electro-capillary effect is in the decrease of the surface tension of a fluid interface by the electric field applied to the interface: the work of the interface charging (produced by external battery) makes negative contribution to the free energy of the interface (Zhang et al., 2001). In our system the NT membrane plays the role of such an interface. The NT membrane can be considered as a cylindrical capacitor charged by the applied field. If we assume that the electrical potential inside the cylinder is uniform and equal to U and the potential of the external media is kept at 0, then the elastic and electric parts of the free energy of the NT can be written as:

$$E_{NT} = 2\,\pi\, r_{NT} L_{NT} \left(\frac{k}{2\, {r_{NT}}^{2}} + \sigma - \frac{C_{sp}\, U^{2}}{2}\right) \qquad \text{(Eq. 3.4)}$$

where C_{sp} is the specific electrical capacitance of the lipid bilayer (1 μF/cm^2). Minimizing E_{NT} with respect to r we obtain:

$$r_{NT} = \sqrt{\frac{k}{2\sigma - C_{SP}\, U^{2}}} = \frac{r_{NTi}}{\sqrt{1 - C_{sp}\, U^{2}/2\,\sigma}} \simeq r_{NTi}\,(1 + C_{sp}\, U^{2}/4\,\sigma) \qquad \text{(Eq. 3.5)}$$

where r_{NTi} is the initial radius of the NT (measured at $U = 0$). We see that in the simplified case of fixed cylindrical geometry the NT expansion effect is proportional to $\frac{C_{sp}\, U^{2}}{\sigma}$. More precise calculations taking into account the changes of the trans-membrane electric field along the NT axis (Figure 3.5) yield:

$$\frac{1}{{r_{NT}}^{2}} = \frac{1}{{r_{NTi}}^{2}} \left(1 - \frac{C_{sp}\, U^{2}/2\,\sigma_{0}}{3}\right) = \frac{2\,\sigma}{k} - \frac{C_{sp}\, U^{2}}{3\,k} \qquad \text{(Eq. 3.6)}$$

Two important conclusions can be made from Eq. 3.6. First, the NT radius does not depend on the NT length even when the shape of the NT deviates from the cylinder, corroborating the experimental observations (Figure 3.4. b). Hence the NT conductance in our experiments is completely determined by the NT length and the effective radius r_{NT}, different at each voltage applied. Secondly, measuring the dependence of r_{NT} on U we can determine the mechanical parameters of the NT membrane, k and σ, in real time (i.e. via application of a voltage ramp), without an *a priori* knowledge of the tension of the parent membrane. Performing such measurements on sGUV system occurred to be a difficult task due to high sensitivity of the system to the applied voltage. Hence we further focus on high-tension BLM system that remains stable even under high (hundreds of mV) holding potentials applied. Besides, the BLM system allows studying submicron NTs suitable for resolving membrane activity of small protein complexes.

3.2. Radius and mechanical parameters of short NTs obtained from BLM

In order to study Dyn1 mediated fission on membrane NTs, the system should approach the molecular dimensions of the fission neck. As it has been demonstrated earlier, such scaling can be archived by using NTs pulled from BLMs, where short (as short as 80nm) and extremely curved (luminal radii of 5-10nm) NTs can be created (Shnyrova et al., 2013). In collaboration with Dr. Pavel Bashkirov (A.N. Frumkin Institute of Physical Chemistry and Electrochemistry, Moscow) we characterized the mechanical parameters of extremely short NTs. Equation 3.6 predicts linear dependence of $\frac{\mathbf{1}}{r_{NT}{}^{2}}$ on U^2 independently on the properties of the parent membrane. Experiments of short non-charged NTs confirmed this theoretical prediction (Figure 3.7.).

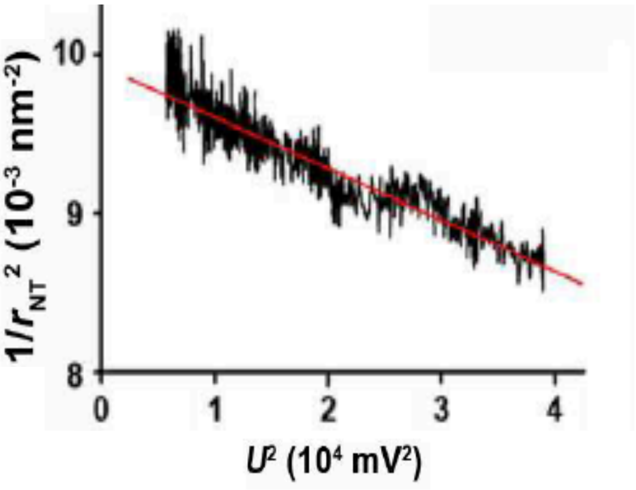

Figure 3.7. Graph $\frac{1}{r_{NT}^2}$ versus U^2 for a NT pulled from BLM and having a constant length L_{NT}. The linear fit to this curve (seen in red) allows for calculating the mechanical parameters of the NT in real time.

We note that the value of the NT radius at 0 voltage can be obtained from the intercept with the Y-axis. Figure 3.7 further demonstrates that the $r_{NT}(U)$ dependence is weak (the radius changes for ~10% when the holding potential increases from 50 to 200mV), justifying quasi-cylindrical approximation of the NT shape used in calculations. However, the electric field produces small but detectable perturbation of the NT shape that can be used to access the elastic constants of the NT membrane in real time.

As it is seen from Equation 3.6, we obtain $\frac{2\,\sigma}{k}$ (defining the NT radius at 0 voltage) from the intercept and $\frac{C_{sp}}{3k}$ from the slope of the fit line shown in Figure 3.7. As C_{sp} is known (directly measurable) parameter, the fit allows recalculation of k and σ.

In collaboration with Dr. Pavel Bashkirov we further obtained the parameters for the NTs made of basic (non-charged) lipid composition and the lipid composition mimicking the inner leaflet of cellular plasma membrane (Table 3.2). We further use this data to quantify membrane-constriction activity of dynamin and its mutants.

Composition	Mol ratio	k (J·10^{-19})
DOPC: DOPE: Chol	40:30:30	0.45 ± 0.04
DOPC: DOPE: Chol: DOPS: PI(4,5)P2	28:25:30:15:2	0.64 ± 0.04

Table 3.2. Bending modulus for different membrane composition of the NT.

3.3. Quantification of membrane deformations during membrane fission mediated by Dyn1

3.3.1. Dyn1 P11C/Y125C Mutant

The main problem in studying the fission process in cells is its ephemeral nature (milliseconds) (Danino et al., 2004) and the short living of its intermediates (microseconds). *In vitro* the situation is similar: while the “preparation” (the NT constriction) is generally long (tens sec, see Figure 2.10. b from Methods chapter) and relatively easy to characterize, the actual membrane rearrangements during fission are extremely fast (ms, see Figure 2.10.b). This makes it very hard to investigate this problem in a real *in vivo* system.

Dynamin is the unique case where we have detailed structural information about transition-state conformation. Our collaborators from UT Southwestern, USA (Dr. Sandra Schmid´s lab) used this information to engineer a dynamin mutant with the idea to “arrest” the transition state conformer of the protein using intra-molecular chemical cross-linking. They created P11C/Y125C double mutant (CC-Dyn1), where one proline in the G domain and a tyrosine in the BSE had been replaced for two cysteines. Cross-linking these cysteines by a short linker molecule (see Methods) stabilizes BSE in its "close" configuration characteristic for the transition state of the GTPase cycle of dynamin (Figure 3.8.).

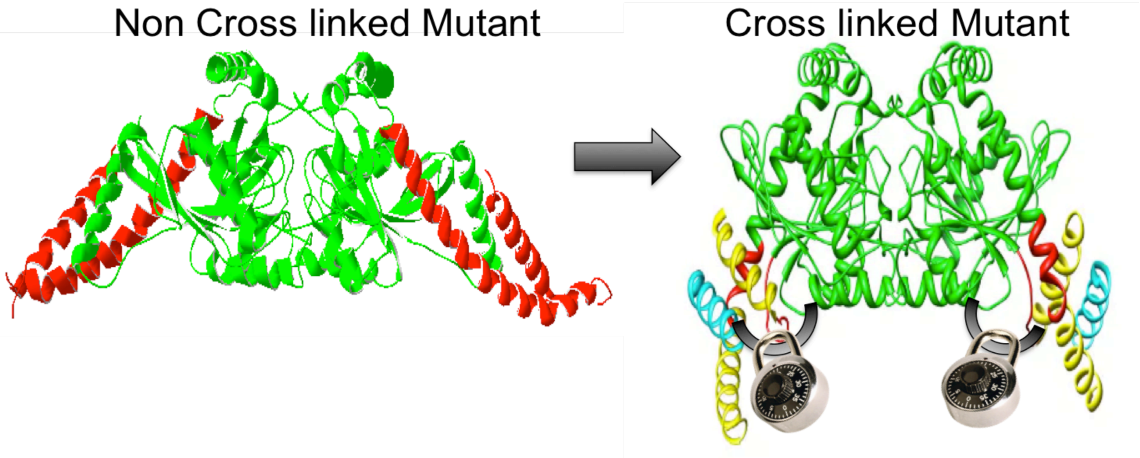

Figure 3.8. Model of G-G dimer (green) and the BSE (red) connector with the stalk in the absence of cross liker (left) and once it has been cross-linked (right). The locks on the left figure symbolize the covalent bounds produced by the crosslinker, thus inhibiting the BSE movement.

We further analysed the membrane activity of the mutated protein in its non-cross-linked (CC-Dyn1) and cross-linked (CxC-Dyn1) forms using our membrane templates.

3.3.2. CC-Dyn1 behaviour on lipid NTs

We first checked whether CC-Dyn1 retains main characteristics of the wild type protein (WT-Dyn1). As WT-Dyn1, CC-Dyn1 produces multiple membrane tubules from flat membrane templates, such as GUVs (see Figure 3.13 upper panel). Next, we measured changes in the electrical conductance of NT induced by CC-Dyn1. The conductance traces observed when 5 μM of CC-Dyn1 where added to the NT closely resembled those recorded in control experiments with wild type protein (Figure 3.9 a). Several conductance steps where observed before the final steady state conductance level, indicating that the complete coverage of the NT by CC-Dyn1 was reached. This behaviour was observed in 11 out of 12 experiments (Figure 3.9 a). In the presence of GTP, membrane constriction produced by CC-Dyn1 is followed by acute conductance drop indicating membrane fission (Figure 3.9 b). Fluorescence microscopy further confirmed that CC Dyn1 severs membrane NTs pulled from GUVs and SUPER templates, further corroborating the notion that CC mutations by themselves do not interfere with the *in vitro* activity of the protein (Figure 3.13, upper panel).

The efficiency of membrane constriction by CC-Dyn1 in the absence of the nucleotide can be calculated from the conductance change (Figure

3.9 a, $G_{initial}$ to G_{final}). If we know the radius of the NT before Dyn1 addition, we obtain the final radius from G_{final}, assuming complete coverage of the tube as:

$$\frac{r_{NT}^{i}}{r_{NT}^{f}} = \sqrt{\frac{G_n^{i}}{G_n^{f}}} \qquad \text{(Eq. 3.7)}$$

The final radius that the NT acquires in the presence of CC-Dyn1 is 2.99±0.95 nm. It coincides with earlier data on WT-Dyn1, corroborating the assumption that CC-Dyn1 operates similarly with WT-Dyn1 on lipid NTs.

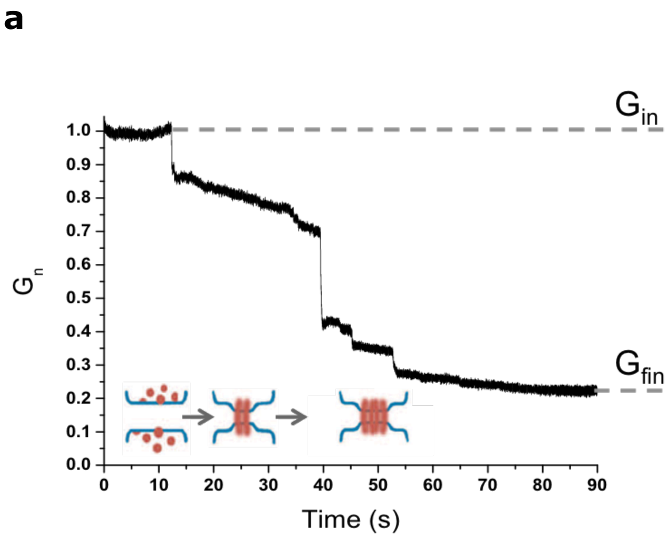

Figure 3.9. Normalized conductance of NT in the presence of CC-Dyn1 mutant.

a) Normalized conductance of NT showing NT constriction (conductance decrease upon CC-Dyn1 addition). The conductance was normalized as $G_n = \frac{G - G_0}{G_i - G_0}$, where G_i is the conductance of the

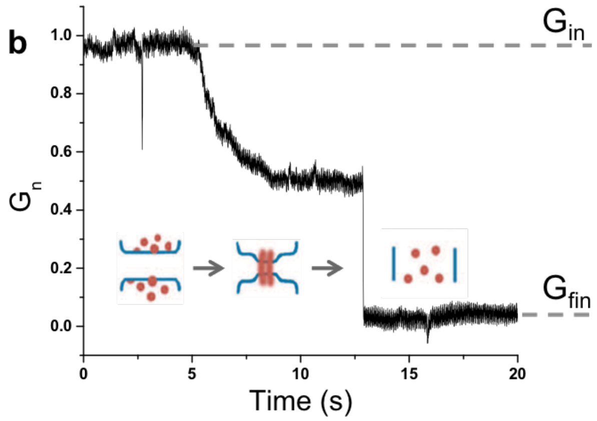

NT before protein addition, and G and G_0 are the measured and the background conductance respectively. G_{fin} corresponds to the stationary scaffold covering the tube. b) Conductance trace showing an example of CC-Dyn1 driven fission of NT in the presence of GTP. $G_{fin} = G_0$

Now, by taking into account the initial NT radius, together with its bending rigidity and tension, determined from the fit of $\frac{1}{r_{NT}^2\,(U^2)}$ (see Figure 3.7.), we can deduce the constriction work that is done by Dyn1 on the membrane.

3.3.3. How much force needs the Dyn1 to bend the membrane of a NT?

As seen in Figure. 3.9. a, the final NT constriction is achieved in tens of seconds. The slow speed of the process (and independence of the constriction rate on the tube length) suggests that the main energy barrier is related to elastic resistance of the lipid bilayer. The change in the elastic part of the free energy can be written as follows:

$$\Delta E_{el} = \Delta E_{\sigma} + \Delta E_{b} = \sigma\,(S_f - S_i) + k\left(\frac{S_f}{r_{NTf}^2} - \frac{S_i}{r_{NTi}^2}\right) \qquad \text{(Eq. 3.8)}$$

where, S_i and S_f are the initial and final area of the NT (the excess of lipids is squeezed to the reservoir membrane), r_{NTi} and r_{NTf} are the initial and final radius of the NT.

$$\Delta E_{el} = 2\pi\sigma L_{NT} r_{NTf}\,(1 - \frac{r_{NTi}}{r_{NTf}}) + 2\pi k L_{NT} r_{NTf}\left(\frac{1}{r_{NTf}^2} - \frac{1}{r_{NTi} r_{NTf}}\right) \qquad \text{(Eq. 3.9)}$$

As we have detailed in the introduction the radius equation is:

$$r_{NT} = \sqrt{\frac{k}{2\,\sigma}} \qquad \text{(Eq. 3.10)}$$

It follows that elastic energy increase per unit area in the final state is:

$$\frac{\Delta E_{el}}{S_f} = 2k\left(\frac{1}{r_{NTf}^2} - \frac{1}{r_{NTi} r_{NTf}}\right) = \frac{2k}{r_{NTf}^2}\left(1 - \frac{r_{NTf}}{r_{NTi}}\right) \qquad \text{(Eq. 3.11)}$$

We want to know the energy per area so for that we will need to take few assumptions depicted in Figure 3.10.

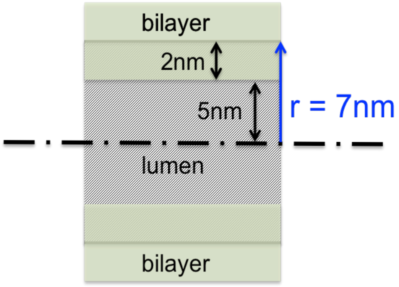

Figure 3.10. Cartoon depicting the geometrical assumptions taken for simplifying the calculations of Dyn1 generated energy per area.

For calculations we take the middle (intermonolayer) plane of the membrane, as is detailed in the Figure 3.10, supposing that the bilayer has no thickness and it is situated in the middle of the bilayer. So, r_{NTi} = 7 nm and r_{NTf} = 4.5 nm. With k = $0.64*10^{-19}$ J = 13k_BT, ΔE_{el} = 0.3k_BT /nm^2. In the final constricted state dynamin polymer is densely packed over the outer monolayer of the constricted NT. The area occupied per dynamin dimer (the structural unit of the polymer) is 24 nm^2 (outer monolayer), corresponding to 16 nm^2 in the middle membrane plane. Hence, the energy generated by dynamin self-assembly and converted into mechanical work of membrane constriction is ~ 5 k_BT per dynamin dimer.

3.3.4. CxC Dyn 1 behaviour on lipid NTs

Cross-linking of CC-Dyn1 stabilizes the protein in its transition-like conformation that was thought to directly produce membrane fission. Corroborating this hypothesis, addition of 5 μM of CxC-Dyn1 to the NT resulted in the closure of the NT lumen in 10 out of 11 cases (Figure 3.11.a), resembling the behaviour of CC-Dyn1 in the presence of GTP. However, in striking contrast with CC-Dyn1+GTP phenotype, no severing of the NT was detected by fluorescence microscopy (Figure 3.11.b).

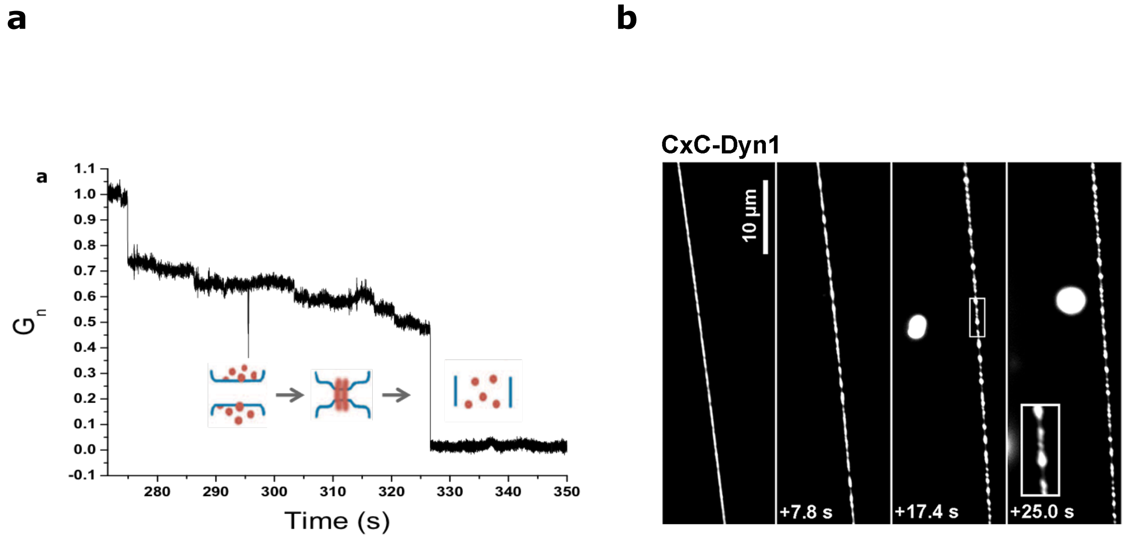

Figure 3.11. Behavior of CxC-Dyn1 on membrane nanotubes. a) Normalized conductance of NT in the presence of CxC-Dyn1 mutant. b) Fluorescence image of NTs in the presence of CxC-Dyn1 showing the absence of NT fission.

Complete closure of the NT lumen without overall disruption of connectivity indicates hemi-fission, the state characterized by disconnection of the inner but not the outer monolayer of the NT (Kozlovsky and Kozlov, 2003). The hemi-fission pathways of membrane remodelling by Dyn1 was previously suggested based upon "non-leaky" character of the fission (Bashkirov et al., 2008): no electrical connection between the exterior and interior of the NT (no leakage) was detected during the membrane remodelling leading to fission. The lack of leakage indicates that the membrane monolayers of the NT break sequentially, not simultaneously, resulting in transient hemi-fission situation.

Another indication of the existence of transient hemi-fission was the reversibility of the NT closure. In earlier experiments with WT Dyn1 it was observed that prior to the complete closure of the lumen, the NT conductance could reversibly switch between "open" and "close" states, a phenomenon known as flicker (Figure 3.12). In the case of CxC-Dyn1, the flicker events were also detected prior complete closure of the NT lumen (in 2 out of 10 experiments). The flicker lasted much longer than for WT-Dyn1 (milliseconds for WT versus seconds for CxC-Dyn1) in agreement with stabilization of the hemi-fission intermediate by CxC-Dyn1 (Figure 3.12).

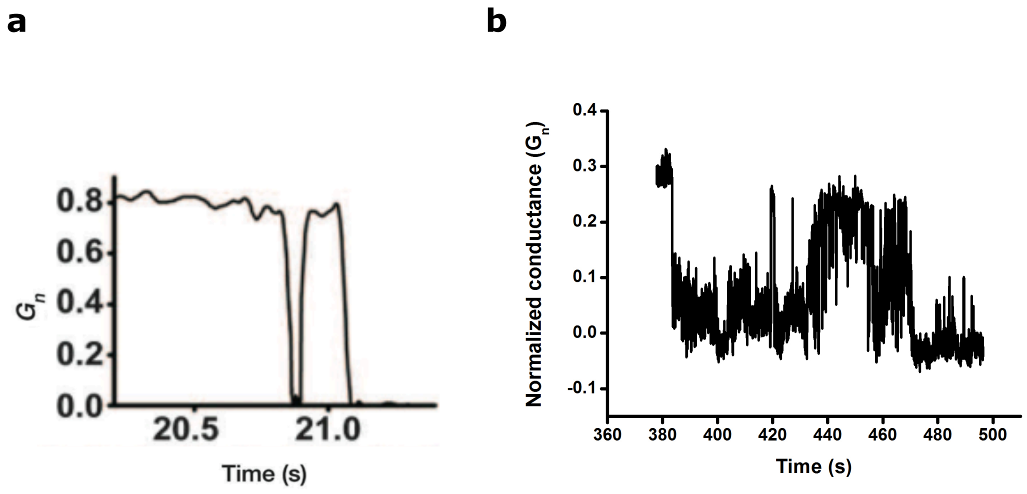

Figure 3.12. Comparison between conductance flickering on background level detected for a) WT-Dyn1 (Shnyrova et al., 2013) and b) CxC-Dyn1.

To directly monitor formation of hemifission, we attempted to apply simultaneous conductance and fluorescence measurements to monitor CxC-Dyn1 interaction with the NTs pulled from sGUVs. However, we found that intrinsic lateral tension of the sGUV system was not sufficient to ensure robust adsorption of the protein (due to low curvature of the NTs). Attempts to augment the tension (e.g. via application of osmotic pressure) made the experiments complex. Although the preliminary dataset supports the existence of hemi-fission, we could not base our final conclusion on this dataset.

The final confirmation of the hemi-fission activity of CxC-Dyn1 came from electron microscopy analysis performed by our collaborators at the National Institutes of Health, USA, Dr. Jenny Hinshaw lab. Cryo EM analysis of CC- and CxC-Dyn1 interaction with LUVs revealed that the inner monolayer of CC Dyn1 covered NTs was always distinguishable, while in the case of the cross-linked protein, the inner monolayer was not distinguishable at some points of the NTs. Hence, stabilization of transition state of Dyn1 produces stable hemifission.

3.3.5. Hemifission separates two mechanistically distinct steps in fission

Next, we studied the activity of CxC-Dyn1 in the presence of GTP. Our collaborators in Dr. Schmid´s lab demonstrated that the membrane-stimulated GTPase activity of CxC-Dyn1 is reduced approximately 10 times as compared to the wild type protein, as the cross-linking seemingly interferes with self-assembly of the protein helix.

First, we confirmed that the GTPase activity of CxC-Dyn1 is preserved on our NTs. We added CxC-Dyn1 to GUVs and recorded the membrane tubulation activity similar to that observed with CC-Dyn1 (Figures 3.13,

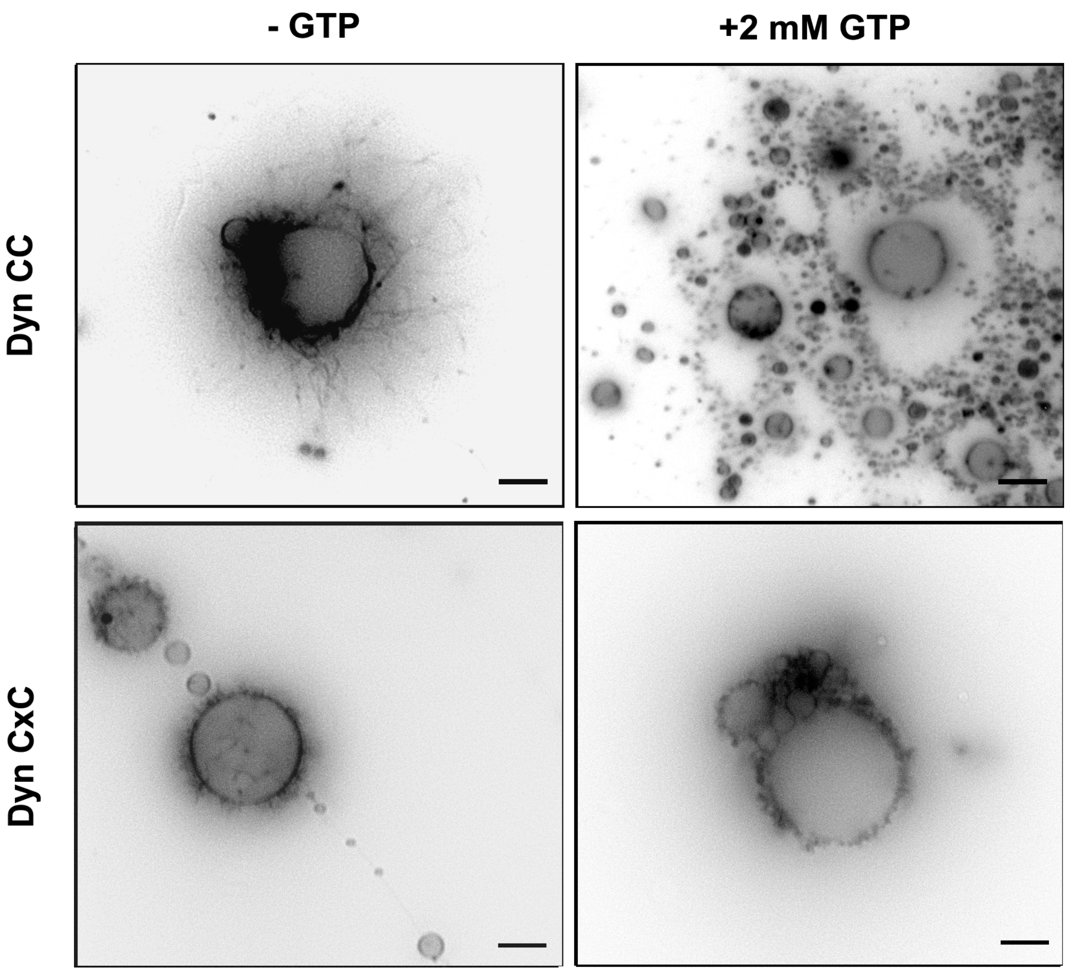

Figure 3.13. Tubulation and tubule retraction by CxC-Dyn1. Upper panel shows fluorescence images showing tubulation (left) and fission of GUVs (right) by CC-Dyn1 in the presence and absence of GTP, respectively. Lower panel shows tubulation of GUVs by CxC-Dyn1 (left) and tubule retraction upon GTP addition (right). Bars 4 μm.

upper panel). Addition of GTP caused fast fragmentation of the tubules produced by CC-Dyn1. No fragmentation but instead retraction of the tubules to the GUV membrane was observed with CxC-Dyn1 (Figure 3.13, lower panel). Hence, CxC-Dyn1 remained responsive to GTP, but the energy of the hydrolysis was not immediately translated into membrane scission.

To investigate the membrane activity of CxC-Dyn1 in details we used short NTs pulled from BLM. Addition of CxC-Dyn1 in the presence of GTP to these NTs resulted in a stationary NT constriction (Figure 3.14, right). The constriction was not followed by the closure of the NT lumen as it was in the absence of the nucleotide (compare Figures 3.11 and 3.14, right). Hence, GTP inhibited the hemi-fission production by CxC-Dyn1 despite the membrane constriction ability of CxC-Dyn1 was preserved. The constriction efficiency of CxC-Dyn1 in the presence of GTP was comparable with that of CC-Dyn1 in the absence of nucleotide: the final conductance levels were 0.22±0.1 for CxC-Dyn1 and 0.27±0.05 for CC-Dyn1. Such a tight membrane constriction is traditionally associated with dynamin polymerization. However, we found a striking difference between the tubes constricted by CC-Dyn1 in the absence of GTP and the tubes constricted by CxC-Dyn1 in the presence of GTP.

CC-Dyn1-covered NTs behaved as if they were covered by a rigid protein scaffolds. When we intended to decrease the length of such tubes by moving the patch pipette towards the BLM, no conductance changes were observed, indicating that the tube length remained fixed. However, the lengthening of the tube resulted in further conductance decrement, demonstrating that electrical connectivity of the tube lumen was preserved (Figure 3.14). Such behaviour was previously reported for WT Dyn1 and was associated with dynamin polymerization (Bashkirov et al., 2008). In turn, CxC-Dyn1-covered tubes behaved essentially similar to pure lipid NTs: their length could be decreased and increased by the patch pipette movement (Figure 3.14). Such behaviour indicates that CxC-Dyn1 forms shorter and/or weaker structure on the NT surface: this "soft" coverage fails to withstand the tube retraction to the parent membrane (driven by the lateral tension), as also seen by fluorescence microscopy (Figure 3.13). The simplest mechanistic explanation of this "softening" is GTP-driven disassembly of dynamin polymer, previously reported for the wild type protein (Bashkirov et al., 2008; Shnyrova et al., 2013).

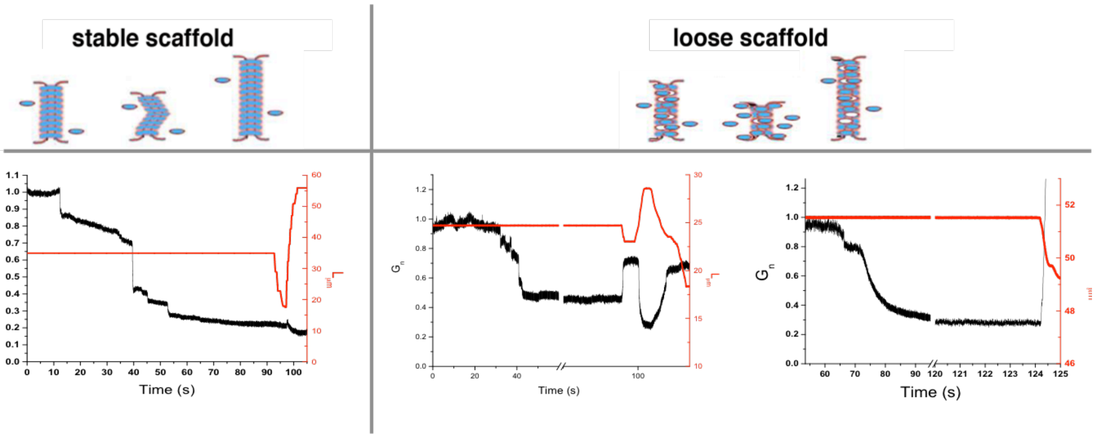

Figure 3.14. Scaffold stability analysis through the conductance data. Left: CC Dyn1 conductance data once the scaffold is around the NT. The black line is the conductance measures and the red one is the length data. When the length in increased (red) more NT is formed and more dynamin is constricting the membrane NT, so the current decreases (black). Right: CXC Dyn1 in the presence of GTP presents a loose scaffold. Those loose scaffolds can maintain the current-length dependence like the upper example or can reach to the NT expansion showing a signal overload.

Such disassembly prevents formation of minimal dynamin scaffolds required to trigger hemi-fission transformation (Shnyrova et al., 2013). But how CxC-Dyn1 produces such a high membrane constriction in the absence of long-range polymerization? Our collaborators from UT Southwestern further revealed that cross-linking affects the positioning of the PH domain of dynamin on the membrane, stabilizing its orientation with maximal membrane insertion (Mehrotra et al., 2014). This augmented insertion is likely responsible for the extreme curvature activity of small oligomers of CxC-Dyn1 forming in the presence of GTP.

To summarize, CxC-Dyn1 produces stable hemifission without using the energy of GTP hydrolysis. Hence, the critical constriction and hemifission of the membrane are not related to the GTPase activity of dynamin. However, the energy of GTP hydrolysis is apparently needed for the transition from hemifission to fission, where Dyn1 further rearrange itself and detaches from the membrane.

Figure 3.15 summarizes our findings on the membrane activity of CC and CxC-Dyn1. We see that cross-linking results in a halting of the fission process at the hemi-fission state. Even addition of GTP to CxC-Dyn1 pre-assembled of the NT fails to convert the hemi-fission produced by CxC-Dyn1 into complete fission.

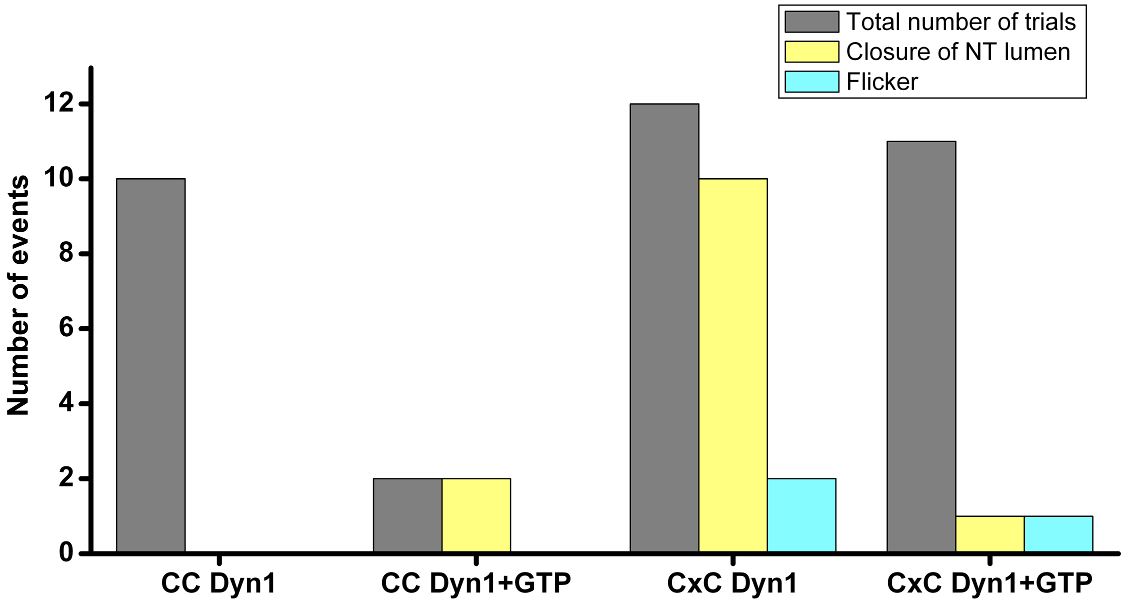

Figure 3.15. Summary of NT conductance measurements results with CC- and CxC-Dyn1.

It has been generally accepted that hemi-fission is an unstable structure characterized by high level of elastic stress (Kozlovsky and Kozlov, 2003). It has also been proposed that simple relaxation of a protein scaffold encaging the hemi-fission intermediate should allow for immediate completion of the fission reaction driven by the elastic stress (Bashkirov et al., 2008). Nevertheless, we found here that depolymerisation of CxC-Dyn1 scaffolds did not lead to complete fission. Rather, depolymerisation impaired even the hemi-fission production by CxC-Dyn1 (Figure 3.14). We conclude that additional energy input is required to convert hemi-fission into complete fission. In case of CxC-Dyn1, this energy cannot be properly translated to the membrane, as the BSE remains locked to the G domain. Hence the coupling between the scaffold disassembly and membrane rearrangements is lost and the fission is inhibited.

Our analysis of the membrane activity of CxC-Dyn1 thus identifies two mechanistically different stages in membrane fission. The first stage is linked to membrane constriction activity of the protein, driven by protein polymerization (curvature scaffolding) and insertion of the protein domains into the membrane. Polymerization is required for assembly of a minimal protein complex that uses the energy of polymerization, membrane insertion and, possibly, nucleotide binding to produce localized membrane constriction resulting in hemifission. The second stage consists in disassembly of the protein complex coupled to rupture of the hemi-fission intermediate. The energy comes from GTP hydrolysis and translated to the membrane via a sequence of conformational rearrangements of the protein. The molecular mechanisms behind hemi-fission to fission transition are to be identified. However, our data demonstrate that even extreme membrane constriction produced by CxC-Dyn1 is not sufficient to ensure this transition. It is likely that the force is to be applied in a different direction (i.e. along the NT axis), as suggested by computer simulations of fission (Fuhrmans and Muller, 2014) and the crucial role of lateral membrane tension in fission (Roux et al., 2006).

3.4. Dyn1 behavior on lipid bilayers supported on surfaced-adhered SiNW

So far we have addressed the membrane activity of dynamin on soft membrane templates. The template geometry is constantly changing during the GTPase cycle of dynamin so that it is practically impossible to separate protein and lipid parts of the system. In order to obtain direct mechanistic insights into mechanics of GTP-driven disassembly of dynamin, we decided to reconstitute this process by using rigid membrane templates. For this purpose, in collaboration with the group of Dr. Alex Noy (Lawrence Livermore National Laboratory, USA), we developed a method of formation of supported lipid bilayer on silicon nanowires templates.

SiNWs are cylindrical wires made of silicon of diameters between 10^{-7} and 10^{-8} m. As described in the Methods Section, we attached the wires to the mica or glass surface and then formed supported lipid bilayer on such composite surfaces. FRAP experiments (conducted in Dr. Noy´s lab) demonstrated that this bilayer is continuous through the SiNW. Hence this membrane template has two essential parts: flat (supported on mica) and curved (supported in the SiNW surface). The bilayer wraps the wires so that the membrane shape at the top of the wire can be approximated by a hemicylinder.

To study interaction of dynamin with the wires we used the wild type protein conjugated with Alexa fluorophores (Dyn-Alexa, Alexa-488 or Alex-647 were used). Dyn-Alexa preferably binds to the membrane supported on the wires, covering completely them. The protein remains bound to the wires after washing off the unbound Dyn-Alexa (Figure 3.16, upper panel). Subsequent addition of GTP to the wires covered by Dyn-Alexa resulted in gradual disappearance of the protein signal while the fluorescence coming from the lipid marker remained practically constant (Figure 3.16, lower panel). This data demonstrate that GTP hydrolysis triggers disassembly of dynamin and further promotes its desorption from the membrane. We plan to further use this template to study the disassembly/desorption process at molecular details using ultra-fast atomic force microscopy (in collaboration with Dr. Noys´lab).

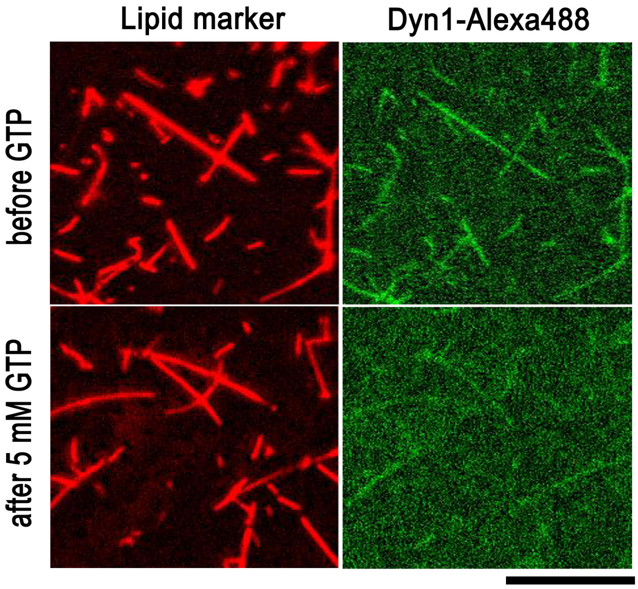
Lipid marker
Dyn1-Alexa488
before GTP
after 5 mM GTP

Figure 3.16. SiNWs covered with lipids and Dyn1 in the absence (upper panel) and presence (lower panel) of GTP. Bar 2 μm.

4. CONCLUSIONS

CONCLUSIONS

- Electro-actuation in lipid nanotubes results in the tube expansion.

- Mechanical parameters (mean curvature, bending modulus and lateral tension) of the nanotube membrane can be determined in real time from the non-linear I/U characteristic of the ionic permeability of the tube lumen.

- Measurements of the nanotube conductance can be used to quantify protein-driven constriction of the tube.

- Protein-driven hemifission can be a stable membrane structure.

- Dyn1-driven hemifission corresponds to the transition state of GTP hydrolysis cycle of the protein.

- The hemifission breaks the fission reaction into two mechanistically different processes.

5. BIBLIOGRAPHY

BIBLIOGRAPHY

Adams, K.L., Engelbrektsson, J., Voinova, M., Zhang, B., Eves, D.J., Karlsson, R., Heien, M.L., Cans, A.S., and Ewing, A.G. (2010). Steady-state electrochemical determination of lipidic nanotube diameter utilizing an artificial cell model. Analytical chemistry *82*, 1020-1026.

Artyukhin, A.B., Shestakov, A., Harper, J., Bakajin, O., Stroeve, P., and Noy, A. (2005). Functional one-dimensional lipid bilayers on carbon nanotube templates. Journal of the American Chemical Society *127*, 7538-7542.

Arumugam, S., and Bassereau, P. (2015). Membrane nanodomains: contribution of curvature and interaction with proteins and cytoskeleton. Essays in biochemistry *57*, 109-119.

Bar-Ziv, R., Moses, E., and Nelson, P. (1998). Dynamic excitations in membranes induced by optical tweezers. Biophysical journal *75*, 294-320.

Bashkirov, P.V. (2006). Membrane Nanotubes in the Electricl Field As a Model for Measurement Parameters of the Lipid Bilayer. Biologieskie Membrany *24*, 183-192.

Bashkirov, P.V., Akimov, S.A., Evseev, A.I., Schmid, S.L., Zimmerberg, J., and Frolov, V.A. (2008). GTPase cycle of dynamin is coupled to membrane squeeze and release, leading to spontaneous fission. Cell *135*, 1276-1286.

Baumgart, T., Hess, S.T., and Webb, W.W. (2003). Imaging coexisting fluid domains in biomembrane models coupling curvature and line tension. Nature *425*, 821-824.

Busse, R.A., Scacioc, A., Hernandez, J.M., Krick, R., Stephan, M., Janshoff, A., Thumm, M., and Kuhnel, K. (2013). Qualitative and quantitative characterization of protein-phosphoinositide interactions with liposome-based methods. Autophagy *9*, 770-777.

Callan-Jones, A., Sorre, B., and Bassereau, P. (2011). Curvature-driven lipid sorting in biomembranes. Cold Spring Harbor perspectives in biology *3*.

Campillo, C., Sens, P., Koster, D., Pontani, L.L., Levy, D., Bassereau, P., Nassoy, P., and Sykes, C. (2013). Unexpected membrane dynamics unveiled by membrane nanotube extrusion. Biophysical journal *104*, 1248-1256.

Cantor, R.S. (1999). The influence of membrane lateral pressures on simple geometric models of protein conformational equilibria. Chemistry and physics of lipids *101*, 45-56.

Carr, J.F., and Hinshaw, J.E. (1997). Dynamin assembles into spirals under physiological salt conditions upon the addition of GDP and gamma-phosphate analogues. The Journal of biological chemistry *272*, 28030-28035.

Chappie, J.S., Acharya, S., Leonard, M., Schmid, S.L., and Dyda, F. (2010). G domain dimerization controls dynamin's assembly-stimulated GTPase activity. Nature *465*, 435-440.

Chappie, J.S., Mears, J.A., Fang, S., Leonard, M., Schmid, S.L., Milligan, R.A., Hinshaw, J.E., and Dyda, F. (2011). A pseudoatomic model of the dynamin polymer identifies a hydrolysis-dependent powerstroke. Cell *147*, 209-222.

Chernomordik, L.V., and Kozlov, M.M. (2003). Protein-lipid interplay in fusion and fission of biological membranes. Annual review of biochemistry *72*, 175-207.

Christensen, S.M., and Stamou, D.G. (2010). Sensing-applications of surface-based single vesicle arrays. Sensors *10*, 11352-11368.

Chung, J., Serezani, C.H., Huang, S.K., Stern, J.N., Keskin, D.B., Jagirdar, R., Brock, T.G., Aronoff, D.M., and Peters-Golden, M. (2008). Rap1 activation is required for Fc gamma receptor-dependent phagocytosis. Journal of immunology *181*, 5501-5509.

Cocucci, E., Gaudin, R., and Kirchhausen, T. (2014). Dynamin recruitment and membrane scission at the neck of a clathrin-coated pit. Molecular biology of the cell *25*, 3595-3609.

Dai, J., and Sheetz, M.P. (1995). Regulation of endocytosis, exocytosis, and shape by membrane tension. Cold Spring Harbor symposia on quantitative biology *60*, 567-571.

Danino, D., and Hinshaw, J.E. (2001). Dynamin family of mechanoenzymes. Current opinion in cell biology *13*, 454-460.

Danino, D., Moon, K.H., and Hinshaw, J.E. (2004). Rapid constriction of lipid bilayers by the mechanochemical enzyme dynamin. Journal of structural biology *147*, 259-267.

Deserno, M. (2014). Fluid lipid membranes: From differential geometry to curvature stresses. Chemistry and physics of lipids.

Dobereiner, H.G., Gompper, G., Haluska, C.K., Kroll, D.M., Petrov, P.G., and Riske, K.A. (2003). Advanced flicker spectroscopy of fluid membranes. Physical review letters *91*, 048301.

Evans, E., Needham, D. (1987). Physical properties of surfactant bilayer membranes: thermal transitions, elasticity, rigidity, cohesion and colloidal interactions. The Journal of physical chemistry *91*, 4219-4228.

Faelber, K., Held, M., Gao, S., Posor, Y., Haucke, V., Noe, F., and Daumke, O. (2012). Structural insights into dynamin-mediated membrane fission. Structure *20*, 1621-1628.

Faelber, K., Posor, Y., Gao, S., Held, M., Roske, Y., Schulze, D., Haucke, V., Noe, F., and Daumke, O. (2011). Crystal structure of nucleotide-free dynamin. Nature *477*, 556-560.

Ferguson, S.M., and De Camilli, P. (2012). Dynamin, a membrane-remodelling GTPase. Nature reviews Molecular cell biology *13*, 75-88.

Ford, M.G., Jenni, S., and Nunnari, J. (2011). The crystal structure of dynamin. Nature *477*, 561-566.

Frolov, V.A., Escalada, A., Akimov, S.A., and Shnyrova, A.V. (2014). Geometry of membrane fission. Chemistry and physics of lipids.

Frolov, V.A., Lizunov, V.A., Dunina-Barkovskaya, A.Y., Samsonov, A.V., and Zimmerberg, J. (2003). Shape bistability of a membrane neck: a toggle switch to control vesicle content release. Proceedings of the National Academy of Sciences of the United States of America *100*, 8698-8703.

Frolov, V.A., Shnyrova, A.V., and Zimmerberg, J. (2011). Lipid polymorphisms and membrane shape. Cold Spring Harbor perspectives in biology *3*, a004747.

Fryer, B. (2004). Micromanager. Harvard business review *82*, 31-34, 135; discussion 136-138, 140.

Fuhrmans, M., and Muller, M. (2014). Coarse-grained simulation of dynamin-mediated fission. Soft matter.

Gallop, J.L., and McMahon, H.T. (2005). BAR domains and membrane curvature: bringing your curves to the BAR. Biochemical Society symposium, 223-231.

Gao, S., von der Malsburg, A., Paeschke, S., Behlke, J., Haller, O., Kochs, G., and Daumke, O. (2010). Structural basis of oligomerization in the stalk region of dynamin-like MxA. Nature *465*, 502-506.

Geng, J., Kim, K., Zhang, J., Escalada, A., Tunuguntla, R., Comolli, L.R., Allen, F.I., Shnyrova, A.V., Cho, K.R., Munoz, D., *et al.* (2014). Stochastic transport through carbon nanotubes in lipid bilayers and live cell membranes. Nature *514*, 612-615.

Grigliatti, T.A., Hall, L., Rosenbluth, R., and Suzuki, D.T. (1973). Temperature-sensitive mutations in Drosophila melanogaster. XIV. A selection of immobile adults. Molecular & general genetics : MGG *120*, 107-114.

Heinrich, M., Tian, A., Esposito, C., and Baumgart, T. (2010). Dynamic sorting of lipids and proteins in membrane tubes with a moving phase boundary. Proceedings of the National Academy of Sciences of the United States of America *107*, 7208-7213.

Heinrich, V., Bozic, B., Svetina, S., and Zeks, B. (1999). Vesicle deformation by an axial load: from elongated shapes to tethered vesicles. Biophysical journal *76*, 2056-2071.

Henriksen, J.R., and Ipsen, J.H. (2002). Thermal undulations of quasi-spherical vesicles stabilized by gravity. The European physical journal E, Soft matter *9*, 365-374.

Henriksen, J.R., and Ipsen, J.H. (2004). Measurement of membrane elasticity by micro-pipette aspiration. The European physical journal E, Soft matter *14*, 149-167.

Heuser, J.E., and Anderson, R.G. (1989). Hypertonic media inhibit receptor-mediated endocytosis by blocking clathrin-coated pit formation. The Journal of cell biology *108*, 389-400.

Hinshaw, J.E., and Schmid, S.L. (1995). Dynamin self-assembles into rings suggesting a mechanism for coated vesicle budding. Nature *374*, 190-192.

Hochmuth, R.M., Mohandas, N., and Blackshear, P.L., Jr. (1973). Measurement of the elastic modulus for red cell membrane using a fluid mechanical technique. Biophysical journal *13*, 747-762.

Hosu, B.G., Sun, M., Marga, F., Grandbois, M., and Forgacs, G. (2007). Eukaryotic membrane tethers revisited using magnetic tweezers. Physical biology *4*, 67-78.

Hsieh, W.T., Hsu, C.J., Capraro, B.R., Wu, T., Chen, C.M., Yang, S., and Baumgart, T. (2012). Curvature sorting of peripheral proteins on solid-supported wavy membranes. Langmuir : the ACS journal of surfaces and colloids *28*, 12838-12843.

Huang, S.C., Artyukhin, A.B., Martinez, J.A., Sirbuly, D.J., Wang, Y., Ju, J.W., Stroeve, P., and Noy, A. (2007). Formation, stability, and mobility of one-dimensional lipid bilayers on polysilicon nanowires. Nano letters *7*, 3355-3359.

Itoh, T., and De Camilli, P. (2006). BAR, F-BAR (EFC) and ENTH/ANTH domains in the regulation of membrane-cytosol interfaces and membrane curvature. Biochimica et biophysica acta *1761*, 897-912.

Jesorka, A., and Orwar, O. (2009). Chapter 15 - Complex nanotube-liposome networks. Methods in enzymology *464*, 309-325.

Koenig, J.H., and Ikeda, K. (1989). Disappearance and reformation of synaptic vesicle membrane upon transmitter release observed under reversible blockage of membrane retrieval. The Journal of neuroscience : the official journal of the Society for Neuroscience *9*, 3844-3860.

Korlach, J., Reichle, C., Muller, T., Schnelle, T., and Webb, W.W. (2005). Trapping, deformation, and rotation of giant unilamellar vesicles in octode dielectrophoretic field cages. Biophysical journal *89*, 554-562.

Koster, G., Cacciuto, A., Derenyi, I., Frenkel, D., and Dogterom, M. (2005). Force barriers for membrane tube formation. Physical review letters *94*, 068101.

Kozlov, M.M. (1999). Dynamin: possible mechanism of "Pinchase" action. Biophysical journal *77*, 604-616.

Kozlov, M.M., Kuzmin, P.I., and Popov, S.V. (1992). Formation of cell protrusions by an electric field: a thermodynamic analysis. European biophysics journal : EBJ *21*, 35-45.

Kozlov, M.M., McMahon, H.T., and Chernomordik, L.V. (2010). Protein-driven membrane stresses in fusion and fission. Trends in biochemical sciences *35*, 699-706.

Kozlovsky, Y., and Kozlov, M.M. (2003). Membrane fission: model for intermediate structures. Biophysical journal *85*, 85-96.

Kulkarni, V.S., Anderson, W.H., and Brown, R.E. (1995). Bilayer nanotubes and helical ribbons formed by hydrated galactosylceramides: acyl chain and headgroup effects. Biophysical journal *69*, 1976-1986.

kwok, R. (1981). Thermoelasticity of Large Lecthin Bilayer Vesicles. Biophysical journal *35*, 637-652.

Liu, Y., and Nagle, J.F. (2004). Diffuse scattering provides material parameters and electron density profiles of biomembranes. Physical review E, Statistical, nonlinear, and soft matter physics *69*, 040901.

Low, H.H., and Lowe, J. (2010). Dynamin architecture--from monomer to polymer. Current opinion in structural biology *20*, 791-798.

Marsh, D. (2006). Elastic curvature constants of lipid monolayers and bilayers. Chemistry and physics of lipids *144*, 146-159.

McMahon, H.T., and Gallop, J.L. (2005). Membrane curvature and mechanisms of dynamic cell membrane remodelling. Nature *438*, 590-596.

McNiven, M.A., Cao, H., Pitts, K.R., and Yoon, Y. (2000). The dynamin family of mechanoenzymes: pinching in new places. Trends in biochemical sciences *25*, 115-120.

Mears, J.A., and Hinshaw, J.E. (2008). Visualization of dynamins. Methods in cell biology *88*, 237-256.

Mehrotra, N., Nichols, J., and Ramachandran, R. (2014). Alternate pleckstrin homology domain orientations regulate dynamin-catalyzed membrane fission. Molecular biology of the cell *25*, 879-890.

Melikyan G. B., A.I.G., Chernomordik L. V., Chailakhyan L.M. (1982). Electrostimulated fusion and fission of bilayer lipid membranes. Biochimica et biophysica acta *730*, 395-398.

Mettlen, M., Pucadyil, T., Ramachandran, R., and Schmid, S.L. (2009). Dissecting dynamin's role in clathrin-mediated endocytosis. Biochemical Society transactions *37*, 1022-1026.

Mim, C., and Unger, V.M. (2012). Membrane curvature and its generation by BAR proteins. Trends in biochemical sciences *37*, 526-533.

Misra, N., Martinez, J.A., Huang, S.C., Wang, Y., Stroeve, P., Grigoropoulos, C.P., and Noy, A. (2009). Bioelectronic silicon nanowire devices using functional membrane proteins. Proceedings of the National Academy of Sciences of the United States of America *106*, 13780-13784.

Morlot, S., Galli, V., Klein, M., Chiaruttini, N., Manzi, J., Humbert, F., Dinis, L., Lenz, M., Cappello, G., and Roux, A. (2012). Membrane shape at the edge of the dynamin helix sets location and duration of the fission reaction. Cell *151*, 619-629.

Mosbacher, J., Langer, M., Horber, J.K., and Sachs, F. (1998). Voltage-dependent membrane displacements measured by atomic force microscopy. The Journal of general physiology *111*, 65-74.

Mueller, P., Rudin, D.O. (1967). Action potential phenomena in experimental bimolecular lipid membranes. Nature *213*, 603-604.

Muhlberg, A.B., Warnock, D.E., and Schmid, S.L. (1997). Domain structure and intramolecular regulation of dynamin GTPase. The EMBO journal *16*, 6676-6683.

Mui, B.L., Dobereiner, H.G., Madden, T.D., and Cullis, P.R. (1995). Influence of transbilayer area asymmetry on the morphology of large unilamellar vesicles. Biophysical journal *69*, 930-941.

Neher, E., Sakmann, B. (1976). Single-channel current recorded from membrane of denervated frog muscle fibres. Nature *260*, 799-802.

Noy, A. (2011). Bionanoelectronics. Advanced materials *23*, 807-820.

Nunez, D., Antonescu, C., Mettlen, M., Liu, A., Schmid, S.L., Loerke, D., and Danuser, G. (2011). Hotspots organize clathrin-mediated endocytosis by efficient recruitment and retention of nucleating resources. Traffic *12*, 1868-1878.

Olbrich, K., Rawicz, W., Needham, D., and Evans, E. (2000). Water permeability and mechanical strength of polyunsaturated lipid bilayers. Biophysical journal *79*, 321-327.

Phillips, M.J., Calero, G., Chan, B., Ramachandran, S., and Cerione, R.A. (2008). Effector proteins exert an important influence on the signaling-active state of the small GTPase Cdc42. The Journal of biological chemistry *283*, 14153-14164.

Powers, T.R., Huber, G., and Goldstein, R.E. (2002). Fluid-membrane tethers: minimal surfaces and elastic boundary layers. Physical review E, Statistical, nonlinear, and soft matter physics *65*, 041901.

Praefcke, G.J., and McMahon, H.T. (2004). The dynamin superfamily: universal membrane tubulation and fission molecules? Nature reviews Molecular cell biology *5*, 133-147.

Pucadyil, T.J., and Schmid, S.L. (2008). Real-time visualization of dynamin-catalyzed membrane fission and vesicle release. Cell *135*, 1263-1275.

Pucadyil, T.J., and Schmid, S.L. (2010). Supported bilayers with excess membrane reservoir: a template for reconstituting membrane budding and fission. Biophysical journal *99*, 517-525.

Quan, A., and Robinson, P.J. (2005). Rapid purification of native dynamin I and colorimetric GTPase assay. Methods in enzymology *404*, 556-569.

Ramachandran, R., Pucadyil, T.J., Liu, Y.W., Acharya, S., Leonard, M., Lukiyanchuk, V., and Schmid, S.L. (2009). Membrane insertion of the pleckstrin homology domain variable loop 1 is critical for dynamin-catalyzed vesicle scission. Molecular biology of the cell *20*, 4630-4639.

Ramachandran, R., Surka, M., Chappie, J.S., Fowler, D.M., Foss, T.R., Song, B.D., and Schmid, S.L. (2007). The dynamin middle domain is critical for tetramerization and higher-order self-assembly. The EMBO journal *26*, 559-566.

Ratinov, V., Plonsky, I., and Zimmerberg, J. (1998). Fusion pore conductance: experimental approaches and theoretical algorithms. Biophysical journal *74*, 2374-2387.

Raucher, D., and Sheetz, M.P. (1999). Characteristics of a membrane reservoir buffering membrane tension. Biophysical journal *77*, 1992-2002.

Reeves, J.P., and Dowben, R.M. (1969). Formation and properties of thin-walled phospholipid vesicles. Journal of cellular physiology *73*, 49-60.

Renard, H.F., Simunovic, M., Lemiere, J., Boucrot, E., Garcia-Castillo, M.D., Arumugam, S., Chambon, V., Lamaze, C., Wunder, C., Kenworthy, A.K.*, et al.* (2015). Endophilin-A2 functions in membrane scission in clathrin-independent endocytosis. Nature *517*, 493-496.

Roux, A. (2013). The physics of membrane tubes: soft templates for studying cellular membranes. Soft matter *9*, 6726-6736.

Roux, A., Cuvelier, D., Nassoy, P., Prost, J., Bassereau, P., and Goud, B. (2005). Role of curvature and phase transition in lipid sorting and fission of membrane tubules. The EMBO journal *24*, 1537-1545.

Roux, A., Koster, G., Lenz, M., Sorre, B., Manneville, J.B., Nassoy, P., and Bassereau, P. (2010). Membrane curvature controls dynamin polymerization. Proceedings of the National Academy of Sciences of the United States of America *107*, 4141-4146.

Roux, A., Uyhazi, K., Frost, A., and De Camilli, P. (2006). GTP-dependent twisting of dynamin implicates constriction and tension in membrane fission. Nature *441*, 528-531.

Salim, K., Bottomley, M.J., Querfurth, E., Zvelebil, M.J., Gout, I., Scaife, R., Margolis, R.L., Gigg, R., Smith, C.I., Driscoll, P.C.*, et al.* (1996). Distinct specificity in the recognition of phosphoinositides by the pleckstrin homology domains of dynamin and Bruton's tyrosine kinase. The EMBO journal *15*, 6241-6250.

Schmid, S.L., and Frolov, V.A. (2011). Dynamin: functional design of a membrane fission catalyst. Annual review of cell and developmental biology *27*, 79-105.

Schneider, C.A., Rasband, W.S., and Eliceiri, K.W. (2012). NIH Image to ImageJ: 25 years of image analysis. Nature methods *9*, 671-675.

Serral, R., Bezlyepkina, N., Knorr, R.L., Lipowsky, R., Dimova, R. (2010). Effect of Cholesterol on the rigidity of saturated and unsaturated membranes: fluctuation and electro-deformation analysis of giant vesicles. Soft matter *6*, 1472-1482.

Sever, S., Damke, H., and Schmid, S.L. (2000). Garrotes, springs, ratchets, and whips: putting dynamin models to the test. Traffic *1*, 385-392.

Shnyrova, A.V., Bashkirov, P.V., Akimov, S.A., Pucadyil, T.J., Zimmerberg, J., Schmid, S.L., and Frolov, V.A. (2013). Geometric catalysis of membrane fission driven by flexible dynamin rings. Science *339*, 1433-1436.

Shpetner, H.S., and Vallee, R.B. (1989). Identification of dynamin, a novel mechanochemical enzyme that mediates interactions between microtubules. Cell *59*, 421-432.

Singh, P., Mahata, P., Baumgart, T., and Das, S.L. (2012). Curvature sorting of proteins on a cylindrical lipid membrane tether connected to a reservoir. Physical review E, Statistical, nonlinear, and soft matter physics *85*, 051906.

Song, B.D., and Schmid, S.L. (2003). A molecular motor or a regulator? Dynamin's in a class of its own. Biochemistry *42*, 1369-1376.

Sorre, B., Callan-Jones, A., Manneville, J.B., Nassoy, P., Joanny, J.F., Prost, J., Goud, B., and Bassereau, P. (2009). Curvature-driven lipid sorting needs proximity to a demixing point and is aided by proteins. Proceedings of the

National Academy of Sciences of the United States of America *106*, 5622-5626.

Steltenkamp, S., Muller, M.M., Deserno, M., Hennesthal, C., Steinem, C., and Janshoff, A. (2006). Mechanical properties of pore-spanning lipid bilayers probed by atomic force microscopy. Biophysical journal *91*, 217-226.

Stepanyants, N., Jeffries, G.D., Orwar, O., and Jesorka, A. (2012). Radial sizing of lipid nanotubes using membrane displacement analysis. Nano letters *12*, 1372-1378.

Stowell, M.H., Marks, B., Wigge, P., and McMahon, H.T. (1999). Nucleotide-dependent conformational changes in dynamin: evidence for a mechanochemical molecular spring. Nature cell biology *1*, 27-32.

Sundborger, A.C., Fang, S., Heymann, J.A., Ray, P., Chappie, J.S., and Hinshaw, J.E. (2014). A dynamin mutant defines a superconstricted prefission state. Cell reports *8*, 734-742.

Svetina, S., and Zeks, B. (2014). Nonlocal membrane bending: a reflection, the facts and its relevance. Advances in colloid and interface science *208*, 189-196.

Sweitzer, S.M., and Hinshaw, J.E. (1998). Dynamin undergoes a GTP-dependent conformational change causing vesiculation. Cell *93*, 1021-1029.

Takei, K., McPherson, P.S., Schmid, S.L., and De Camilli, P. (1995). Tubular membrane invaginations coated by dynamin rings are induced by GTP-gamma S in nerve terminals. Nature *374*, 186-190.

Tian, A., Capraro, B.R., Esposito, C., and Baumgart, T. (2009). Bending stiffness depends on curvature of ternary lipid mixture tubular membranes. Biophysical journal *97*, 1636-1646.

Tunuguntla, R.H., Bangar, M.A., Kim, K., Stroeve, P., Grigoropoulos, C., Ajo-Franklin, C.M., and Noy, A. (2014). Bioelectronic Light-Gated Transistors with Biologically Tunable Performance. Advanced materials.

Tunuguntla, R.H., Bangar, M.A., Kim, K., Stroeve, P., Grigoropoulos, C., Ajo-Franklin, C.M., and Noy, A. (2015). Bioelectronic light-gated transistors with biologically tunable performance. Advanced materials *27*, 831-836.

van der Bliek, A.M. (1999). Functional diversity in the dynamin family. Trends in cell biology *9*, 96-102.

Varkey, J., Isas, J.M., Mizuno, N., Jensen, M.B., Bhatia, V.K., Jao, C.C., Petrlova, J., Voss, J.C., Stamou, D.G., Steven, A.C.*, et al.* (2010). Membrane curvature induction and tubulation are common features of synucleins and apolipoproteins. The Journal of biological chemistry *285*, 32486-32493.

Warnock, D.E., Hinshaw, J.E., and Schmid, S.L. (1996). Dynamin self-assembly stimulates its GTPase activity. The Journal of biological chemistry *271*, 22310-22314.

Waugh, R. (1979). Thermoelasticity of Red Blood Cell Membrane. Biophysical journal *26*, 115-132.

Waugh, R. (1982). Surface Viscosity Measurements from Large Bilayer Vesicle Tether Fromation. Biophysical journal *38*, 29-37.

Zhang, P., and Hinshaw, J.E. (2001). Three-dimensional reconstruction of dynamin in the constricted state. Nature cell biology *3*, 922-926.

Zhang, P.C., Keleshian, A.M., and Sachs, F. (2001). Voltage-induced membrane movement. Nature *413*, 428-432.

Zilker, A., Ziegler, M., and Sackmann, E. (1992). Spectral analysis of erythrocyte flickering in the 0.3-4- microm-1 regime by microinterferometry combined with fast image processing. Physical review A *46*, 7998-8001.

Zimmerberg, J., and Kozlov, M.M. (2006). How proteins produce cellular membrane curvature. Nature reviews Molecular cell biology *7*, 9-19.

6. RESUMEN Y CONCLUSIONES

6.1. Resumen

En los últimos años se ha ido desvelando el rol activo de la curvatura de membrana en los procesos de reorganización de membranas celulares. La mayoría de las membranas celulares presentan una cierta curvatura; dicha curvatura es moderada en los casos de orgánulos tubulares e incluso puede llegar a ser una curvatura extrema como es el caso de los poros de fisión y fusión. Experimentos *in vitro* en pequeñas vesículas unilamelares (SUVs) o nanotubos lipídicos (NTs) muestran la efectividad de la curvatura de membrana en la segregación lipídica y formación de dominios activos en transformaciones morfológicas.

El trabajo en esta tesis ha consistido en desarrollar herramientas *in vitro* que nos ayuden a estudiar los procesos de elevada curvatura con la adecuada resolución espacial y temporal, y a su vez que nos permitan esclarecer los mecanismos de creación de curvatura de membrana y los procesos de la remodelación celular. Los patrones lipídicos utilizados se pueden dividir en patrones blandos (NTs lipidicos) o patrones rígidos (nanoalambres de silicio (SiNWs) cubiertos de membrana).

Los NT blandos utilizados poseen un diámetro luminal de varias decenas de nanómetros y pueden tener desde unas decenas de nanómetros hasta micras de longitud. Los nanotubos más largos obtenidos a partir de vesículas gigantes (GUVs), son más anchos pero permiten la visualización simultanea por microscopía de fluorescencia. Los nanotubos más cortos son obtenidos a partir de bicapas lipídicas negras (BLMs), con mayor tensión que los GUVs, por lo que poseen unos radios muy reducidos.

La diferencia de radios de los NTs son el resultado de diversos parámetros mecánicos de la membrana que forma el tubo. Los parámetros mecánicos que definen la geometría del NT son la rigidez a la flexión (k, definida por la composición lipídica) y la tensión lateral de la membrana (σ). En este trabajo la composición lipídica fue idéntica tanto para los GUVs como para las BLMs, por lo que el radio de los NTs estaba regulado tan sólo por la tensión lateral de la membrana origen.

La determinación cuantitativa de los radios de los NTs se hace mediante el paso de una corriente eléctrica por el interior del NT de membrana. El NT de membrana ofrece una resistencia al paso de la corriente que es función del área de la sección transversal del mismo, de tal forma que existe una dependencia del radio del NT y de su longitud. Al incrementar o empequeñecer la longitud del NT obtenemos una respuesta en la medida de conductancia reduciéndose o agrandándose ésta. De esta forma se puede hallar el radio del NT.

Para los NTs obtenidos a partir de GUVs se determinó que el voltaje afecta la forma del NT, dejando éste de ser cilíndrico. Se determina en este trabajo que el radio del NT sufre una desviación $\frac{C_{sp}\,U^2}{6\,\sigma}$ que depende de la longitud total del NT. De tal forma que el gradiente de voltaje que existe en el tubo origina una variación en la tensión lateral y esto da como resultado una forma de "trompeta" en el NT.

Las medidas de conductancia sobre un NT permiten calcular en tiempo real y simultáneamente los parámetros mecánicos de la membrana del NT. Se procede al calculo de dichos parámetros para varias composiciones lipídicas conocidas en la literatura actual

Como se puede apreciar en lo anteriormente descrito, esta técnica ofrece una medida directa de la geometría del NT así como de los parámetros mecánicos que la determinan y sirve como una inestimable ayuda para el estudio de la creación de nuevos compartimentos de membrana promovidos por la presencia de proteínas de fisión.

La segunda parte de esta tesis está dedicada al estudio del proceso de fisión promovido por la proteína dinamina I (Dyn1), siendo ésta el prototipo de proteína de fisión. La Dyn1 es una guanosina-5'-trifosfatasa (GTPasa) de casi 900 amino ácidos y 100 KDa. La Dyn1 es la proteína de fisión más estudiada ya que esta íntimamente envuelta en los procesos de endocitosis mediados por la clatrina. Se sabe que precisamente la Dyn1 es la responsable de la fisión de las vesículas en estos procesos.

Sobre el *modus operandi* de la Dyn 1 *in vivo* se sabe que necesita la existencia de un cuello de membrana de elevada curvatura (cuello mimetizado *in vitro* por un NT) para polimerizar sus monómeros alrededor de este, hidrolizar las moléculas de guanosina-5'-trifosfato (GTP) y por último gestionar la fisión de la membrana. En este trabajo se hacen referencia a dos de los diferentes estados conformacionales de la Dyn1, uno el estado en el que el polímero se ha enlazado a la molécula de GTP y lo llamaremos de aquí en adelante **estado basal** y un segundo estado pre-hidrólisis en el que la Dyn 1 sigue enlazada al guanosina difosfato (GDP) y al P que se llamará **estado de transición**. La naturaleza efímera de éstos estados imposibilita el estudio de estas configuraciones transitorias. Para posibilitar la obtención de información debemos de parar el proceso en estos estadios. Usando una mutación de la Dyn1 en combinación con de una fijación química (crosslinker), nuestros colaboradores (Laboratorio de la Dra. Sandra Schmid, en UT Southwestern, Texas, EEUU) han conseguido crear una mutante del estado de transición de la Dyn1. Ello nos permitió estudiar el papel que juega esta configuración de la proteína en el proceso de fisión de la membrana. Cuando este mutante se añadió a los NT blandos, se observó la formación de un estado de hemifisión de la membrana, que nunca antes se había detectado *in vitro*. Cabe destacar que la formación del estado de hemifisión de la membrana sólo fue posible en ausencia de GTP. La adición de GTP promovió la desestabilización del andamiaje de la dinamina, disminuyendo su capacidad de constricción de la membrana. Todo ello, unido a datos obtenidos por técnicas complementarias permitió proponer un mecanismo detallado de la fisión de la membrana por la dinamina, donde se da gran importancia a la inserción coordinada de los dominios PH de la dinamina dentro de la membrana para la formación del estado de hemifisión. La fisión completa es una consecuencia de la hidrólisis del GTP por la proteína y del desensamblaje del polímero de dynamina sobre la membrana.

En la última parte de la tesis se ha estudiado la interacción de la Dyn1 con los NT rígidos formados por nanoalambres de silicona recubierdos de bicapa lipídica. Éstas plantillas además de ser rígidas presentan la forma de hemicilindro, por lo que la dinamina no puede ensamblarse en un circulo completo encima de ellas. Se observó la formación de oligómeros de Dyn1 encima de éstos hemicilindros. Además, éstos oligómeros preservan la habilidad de hidrolizar GTP. El rol de estos oligomeros *in vivo* se aclarará en futuros estudios.

6.2. Conclusiones

- La electro-actuación provoca la expansión de los nanotubos lipídicos.

- Los parámetros mecánicos de los nanotubos de membrana (resistencia al doblamiento y tensión lateral) se pueden determinar en tiempo real usando la característica I/U no-linear de la permeabilidad iónica del lumen del nanotubo lipídico.

- Las medidas de la conductancia del nanotubo se pueden usar para la cuantificación de la constricción del nanotubo promovida por proteínas.

- La hemifisión de membrana creada por proteínas puede ser una estructura de membrana estable.

- La hemifisión de membrana promovida por la Dyn1 corresponde al estado de transición del ciclo de la hidrólisis del GTP.

- La hemifisión rompe la reacción de fisión en dos procesos mecanísticamente diferentes.